



POLITECNICO
MILANO 1863

SCUOLA DI INGEGNERIA INDUSTRIALE
E DELL'INFORMAZIONE

Qualitative study of ballistic capture at Mars via Lagrangian descriptors

TESI DI LAUREA MAGISTRALE IN
SPACE ENGINEERING - INGEGNERIA SPAZIALE

Author: **Alessio Quinci**

Student ID: 944660

Advisor: Prof. Francesco Topputo

Co-advisor: Gianmario Merisio

Academic Year: 2020-21

Abstract

A new approach to design ballistic capture orbits can be found within the field of fluid dynamics. Lagrangian coherent structures are time-evolving structures in the phase space of a generic dynamical system which separate regions with qualitatively different dynamic behaviour. Lagrangian descriptors represent a novel approach to highlight the geometrical template of phase space structures. They have already found a myriad of applications in different areas such as ocean currents, marine oil spills, atmospheric sciences and chemistry.

This study presents a new technique based on Lagrangian descriptors applied to ballistic capture design. The research purpose is to exhibit to what extent descriptors give information about non-Keplerian dynamics in Mars proximity. Motivations rely on the fact that Lagrangian descriptors have the potential to be an efficient and easy to be implemented visual tool that could give a richer understanding of dynamics around the target planet compared with stable sets manipulation techniques.

The methodology described in this thesis aims to show the correlation between the dynamics separatrices generated in the Lagrangian descriptor fields and the weak stability boundary of stable sets. Separatrices are extracted from the descriptor fields with an edge detection algorithm. Results demonstrated the ability of the descriptors to distinguish phase space regions of initial conditions around Mars that generate orbits with different qualitative behaviour. Lagrangian descriptors proved to be an useful and intuitive tool to aid in the design of ballistic capture orbits.

Keywords: Planar elliptic restricted three-body problem; Lagrangian descriptors; Ballistic capture; Mars.

Sommario

Un nuovo approccio alla progettazione di orbite di cattura gravitazionale può essere trovato nel campo della fluidodinamica. Le strutture coerenti di Lagrange sono strutture tempo-varianti nello spazio delle fasi di un sistema dinamico generico, che separano regioni con comportamenti dinamici qualitativamente diversi. I descrittori di Lagrange rappresentano un nuovo approccio atto ad evidenziare il profilo geometrico delle strutture nello spazio delle fasi. Essi hanno già trovato una miriade di applicazioni in diverse aree come le correnti oceaniche, le fuoriuscite di petrolio nel mare, le scienze atmosferiche e la chimica.

Questo studio presenta una nuova tecnica basata sui descrittori di Lagrange applicata al design della cattura gravitazionale. Lo scopo della ricerca è mostrare fino a che punto i descrittori forniscano informazioni sulla dinamica non Kepleriana in prossimità di Marte. Le motivazioni si basano sul fatto che i descrittori di Lagrange hanno il potenziale per essere uno strumento visivo efficiente e facile da implementare, che potrebbe fornire una comprensione più ricca della dinamica attorno al pianeta rispetto alle tecniche di manipolazione dei set stabili.

La metodologia descritta in questa tesi mira a mostrare la correlazione tra le separatrici della dinamica generate nei campi dei descrittori di Lagrange e i confini dei set stabili. Le separatrici sono estratte attraverso un algoritmo di rilevazione delle discontinuità nel campo del descrittore. I risultati hanno mostrato la capacità dei descrittori nel distinguere regioni di condizioni iniziali nello spazio delle fasi attorno a Marte che generano orbite con differenti comportamenti dinamici. I descrittori di Lagrange si sono rivelati uno strumento utile e intuitivo che aiuta nella progettazione di orbite di cattura gravitazionale.

Parole chiave: Problema piano ellittico ristretto dei tre corpi; Descrittori di Lagrange; Cattura gravitazionale; Marte.

Acknowledgements

First of all, I would like to express gratitude to my advisor Prof. Francesco Topputo, who gave me the possibility to explore this stimulating topic. He gave me confidence and complete support. Then, I would thank Gianmario Merisio for his valuable advices, for being always available and patient.

My gratitude also goes out to my colleagues, friends and roommates who enriched my days all along the journey. Finally, I would thank my parents for their unconditional love.

Contents

Abstract	i
Sommario	iii
Acknowledgements	v
Contents	vii
List of figures	ix
List of tables	xi
List of abbreviations	xiii
List of symbols	xv
1 Introduction	1
1.1 Context	1
1.2 Motivations	2
1.3 Research question and objectives	3
1.4 Structure of the thesis	4
2 Dynamical models	5
2.1 Planar circular restricted three-body problem	5
2.1.1 Invariant manifolds	7
2.2 Planar elliptic restricted three-body problem	11
3 Ballistic capture	13
3.1 Orbits classification	13
3.2 Design of ballistic capture orbits	17

4	Lagrangian coherent structures	19
4.1	Definition and properties	19
4.2	Variational equations	21
4.3	Finite-time Lyapunov exponent	22
4.4	Variational theory	25
4.5	Lagrangian descriptors	28
4.6	The Duffing oscillator example	31
4.7	Applications to ballistic capture	33
4.8	LCSs extraction strategies trade-off	35
5	Ballistic capture at Mars via Lagrangian descriptors	37
5.1	Definition of classification sets	37
5.2	Lagrangian descriptors computation	39
5.2.1	Consideration on the integration limits	41
5.3	Separatrices extraction	44
5.4	Validation of extracted separatrices	45
6	Results	49
6.1	Classification sets	49
6.2	Lagrangian descriptor fields	51
6.3	Extracted separatrices	55
6.4	Validation	58
7	Conclusions	65
A	LD fields symmetry	67
	Bibliography	69

List of figures

1.1	Transfers to the Moon.	2
2.1	Synodic coordinate frame.	6
2.2	Equilibrium points of the CR3BP in the synodic frame.	7
2.3	Invariant manifolds of a Lyapunov orbit about L_1 for a given energy.	8
2.4	The four Poincaré sections U_i in the Sun–Jupiter system.	9
2.5	Position space projection of the L_1 and L_2 periodic orbit manifold tubes.	10
2.6	An itinerary region (X, J, S)	10
2.7	Elliptical orbits of primaries.	11
2.8	Pulsating Hill’s curves in the ER3BP.	12
3.1	Intersection plane and orbit categories.	15
3.2	Sample orbits around Mercury.	16
3.3	Sample orbit about Mercury of \mathcal{C}_{-1}^6 capture set.	17
3.4	Sample solution of an Earth–Mars transfer in \mathcal{C}_{-1}^6	18
4.1	Material surface evolution in the extended phase space.	20
4.2	Hyperbolic LCSs.	20
4.3	Repelling and attracting LCS candidates for a vortex behind a cylinder.	23
4.4	Two points on opposite sides of a stable manifold.	23
4.5	Double gyre phase space structures.	25
4.6	Evolving material surface $\mathcal{M}(t)$	26
4.7	The role of coherent structures in stretching (a) and folding (b).	27
4.8	Stable and unstable manifolds of Duffing oscillator.	31
4.9	FTLE fields of Duffing oscillator.	32
4.10	LD field of forced Duffing oscillator.	32
4.11	Invariant manifolds intersections in the CR3BP.	33
4.12	FTLE field for the Sun–Mars ER3BP and $\mathcal{W}_1(0, 0.9)$ comparison.	34
4.13	Repelling LCS overlapped to stable sets of Sun–Mars system.	34
5.1	Synodic reference frame and polar coordinates.	39

5.2	Stable sets of Sun–Mars ER3BP.	41
5.3	Final anomaly functions.	43
5.4	M_1 contour plots for different f_f functions.	43
5.5	$M_4(G, 0, 200\sqrt{r_0}, 0)$	43
5.6	Validation workflow.	45
5.7	Coordinates transformation.	46
6.1	Computational grid classification for different values of f_f	50
6.2	Two capture sets.	51
6.3	Comparison between LD fields computed for the same integration interval.	52
6.4	Scaled M_2 and M_4 fields.	53
6.5	$M_3(G, f_0, f_F, f_B)$ fields.	54
6.6	Edge detection methods comparison.	56
6.7	$M_3(G, f_0, f_F, f_B)$ fields with extracted separatrices.	57
6.8	Extracted separatrices overlapped to subsets for different final anomalies.	59
6.9	Extracted separatrices overlapped to capture sets.	60
6.10	Orbits generated from samples "a" to "f" in Tab. 6.2.	61
6.11	Orbits generated from samples "g" to "l" in Tab. 6.2.	62

List of tables

2.1	Normalization units.	5
4.1	Performance comparison between LCSs extraction techniques.	35
5.1	Implemented Lagrangian descriptors.	40
5.2	Parameters for the computation of the initial states and physical parameters.	47
6.1	Computed descriptor fields and associated thresholds.	55
6.2	Initial conditions sampled from Figs. 6.8 and 6.9.	63

List of abbreviations

CG	Cauchy-Green.
CR3BP	circular restricted three-body problem.
ER3BP	elliptic restricted three-body problem.
FTLE	finite-time Lyapunov exponent.
IC	initial condition.
LCS	Lagrangian coherent structure.
LD	Lagrangian descriptor.
SOI	sphere of influence.
STM	state transition matrix.
WSB	weak stability boundary.

List of symbols

ξ_i	Cauchy-Green strain tensor eigenvectors
λ_i	Cauchy-Green strain tensor eigenvalues
Δ	Cauchy-Green strain tensor
Φ	State transition matrix
\mathbf{A}	Jacobian of the flow
\mathbf{x}	State vector
\mathcal{C}	Capture set
\mathcal{K}	Crash set
\mathcal{M}	Material surface
\mathcal{W}	Weakly stable set
\mathcal{X}	Escape set
μ	Mass parameter
$\nu_{t_0}^t$	Repulsion ratio
Ω	Potential of the circular problem
ω	Potential of the elliptic problem
$\phi_{t_0}^t$	Flow map
$\rho_{t_0}^t$	Normal repulsion rate
$\sigma_{t_0}^T$	Finite-time Lyapunov exponent
\tilde{x}, \tilde{y}	P coordinates in the inertial frame
a_p	Semi-major axis of P_1 – P_2 system
e	Eccentricity of P initial osculating orbit

e_p	Eccentricity of P_1 - P_2 system
f	True anomaly of P_2
G	Computational grid of the initial states
H	Kepler energy of P relative to P_2
J_C	Jacobi integral of the circular problem
J_E	Jacobi integral of the elliptic problem
L_i	Lagrangian points
M_i	Lagrangian descriptors
m_i	Mass of primaries ($i = 1, 2$)
n	Stability number
P	Third body
P_i	Primaries ($i = 1, 2$)
r, θ	P polar coordinates in the synodic frame centered at P_2
R_{12}	P_1 - P_2 distance
R_{eq}	Mean equatorial radius of P_2
R_s	Sphere of influence radius of P_2
t	Time
U_i	Poincaré sections
W^s, W^u	Stable and unstable manifolds
x, y	P coordinates in the synodic frame

1 | Introduction

1.1. Context

Ballistic capture transfers have been receiving increasing attention throughout the past few decades. They forsake the classic Keplerian approach typical of an Hohmann transfer and exploit in a natural way gravitational forces exerted simultaneously by solar system bodies on the spacecraft. Ballistic capture orbits have the capability to reduce fuel requirements and to provide more flexibility in terms of insertion opportunities and launch windows [24]. A temporary capture orbit can provide multiple insertion opportunities into stable orbits about the target body, mitigating single-point failure risks [23]. Ballistic capture orbits are only temporary and after a finite amount of time the spacecraft escapes the target body or crashes on its surface. In order to have a controlled capture some sort of energy dissipation must be introduced. This could be dealt with thrusting manoeuvres or aerobraking [25]. Ballistic capture orbits are a family of low-energy transfer trajectories. In the context of interplanetary transfers, compared with Hohmann trajectories, they reduce the relative hyperbolic excess velocity upon arrival between the spacecraft and the target planet typical of a patched-conics Keplerian approach. Lower energy is needed to stabilize the spacecraft on its final orbit around the target [19]. Summing up, the advantages as compared to a traditional patched-conics transfer are:

- reduction of propellant mass for the insertion manoeuvres at arrival primary;
- reduction of single-point failure risks;
- wider launch windows.

The qualitative difference in trajectory between an Hohmann transfer and a ballistic capture orbit in the Earth–Moon system can be appreciated in Fig. 1.1. In the case of ballistic transfer, the manoeuvre (ΔV_2) is performed far from the target. Starting from the manoeuvre point, the spacecraft will naturally be captured by the Moon gravitational influence. Propellant consumption for the ballistic capture orbit is less than that for the Hohmann transfer [21].

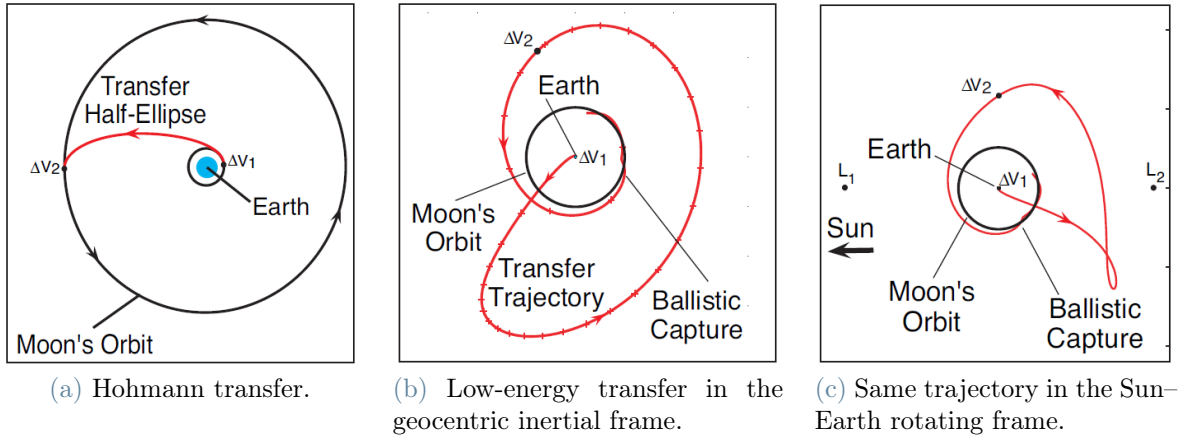


Figure 1.1: Transfers to the Moon [21].

The first ballistic capture attempt has been done in 1991, when the Japanese Hiten mission used a low energy transfer to reach the Moon exploiting the combined gravitational effects of the Earth, the Moon, and the Sun [3]. A standard Hohmann transfer was not possible since not sufficient fuel was available, so for the first time the feasibility of ballistic capture has been demonstrated. The transfer required five months instead of the usual three days of an impulsive strategy. Since Hiten, other space missions employed ballistic trajectories, such as SMART-1 [34] and GRAIL [18]. Ballistic capture has also been implemented as design solution in BepiColombo mission [20], Lunette [6], ESMO [40], to the Jupiter moons [4], and in asteroid retrieval contexts [38].

1.2. Motivations

The design of a ballistic capture orbit can be performed by following two different philosophies [19]. One of them is the exploitation of invariant manifolds of periodic orbits in the circular restricted three-body problem (CR3BP). This strategy allows to design trajectories with prescribed behaviour. As an advantage, this method gives insight into the dynamics of the capture. However, there is no control on orbital elements of final arrival orbit and the method is only applicable in the CR3BP.

The other design strategy is based on stable sets manipulation. Stable sets are sets of initial conditions (ICs) in the phase space of a dynamical system whose generated trajectories satisfy certain stability conditions. The method is attractive because it does not require deep knowledge of the dynamics in proximity of target primary. Moreover, stability definitions can be extended to arbitrary complex, non-autonomous models. The main drawback is the brute-force nature of the method which is in general more computation-

ally intensive than invariant manifolds computation. Stable sets manipulation technique will be addressed in more details in Chapter 3.

A novel approach to aid in the design of ballistic capture orbits may be found in fluid dynamics, from which the concept of Lagrangian coherent structures (LCSs) arises [14]. LCSs are structures in the phase space of a dynamical system separating regions in which the flow has different behaviour. This new concept may allow for a more rich understanding of the dynamics about the arrival planet, and offer a fresh perspective on the ballistic capture mechanism. Another important advantage is that LCS-based strategies can be applied to non-autonomous dynamical systems. For instance, in astrodynamics, they permit to take into account for third-body perturbations, solar radiation pressure, or non-spherical gravity perturbations. In previous studies, LCS-based techniques were already applied to get insight on the ballistic capture problem [28, 31, 33, 41]. It has been shown that LCSs computed around a planet are linked to the weak stability boundary (WSB) of stable sets.

Lagrangian descriptors (LDs) were recently introduced as a powerful tool capable of unveiling LCSs and therefore highlighting geometrical structures that act as dynamics separatrices [27]. LDs seem to have all the credentials to help in the design of ballistic orbits and enrich the dynamics knowledge in proximity of the target planet compared with previously mentioned design philosophies.

1.3. Research question and objectives

This thesis aims to validate LDs as an approach capable of providing a qualitative picture of the dynamical environment about Mars in relation to ballistic capture orbits. In particular, the study wants to answer the following research question:

To what extent Lagrangian descriptors provide a characterization of the dynamics in Mars proximity with regard to ballistic capture?

Following the research question, the main thesis objectives are:

- computation of the LDs fields associated to a phase space region around Mars;
- selection of the most suited LD;
- extraction of the phase space structures acting as dynamics separatrices from the LD fields;
- verification of the correlation between highlighted regions and classification sets, and extracted separatrices and WSBs.

1.4. Structure of the thesis

The present thesis is organized as follows:

- Chapter 1 gives a general background of ballistic capture and design strategies. It introduces LCSs approach as viable strategy for the design. It presents the research question and objectives of the thesis.
- Chapter 2 describes dynamical models used in the developed methodology.
- Chapter 3 focuses on stable sets manipulation as design strategy for a ballistic capture orbit.
- Chapter 4 defines LCSs together with the strategies to locate them in the phase space of a generic dynamical system. Different approaches are tested on a toy problem.
- Chapter 5 presents the methodology developed to extract and validate the separatrices from the LD fields computed in the proximity of Mars when facing the ballistic capture problem.
- Chapter 6 summarizes the results of this study.
- Chapter 7 elaborates on the final remarks. In particular, the research question is answered, advantages and limitations of the LD-based strategy applied to the design of ballistic capture orbits are discussed, and recommendations for future works are provided.

2 | Dynamical models

The methodology developed in this study and presented in Chapter 5 assumes the planar elliptic restricted three-body problem (ER3BP) as a reference dynamical model. In this chapter a description of the CR3BP and ER3BP models is given. The latter can be considered a natural generalization of the circular problem.

2.1. Planar circular restricted three-body problem

The CR3BP describes the motion of a particle P of negligible mass moving under the gravitational influence of two primary masses m_1 and m_2 , with $m_1 \geq m_2$ [21]. Primaries P_1 and P_2 move on circular orbits around their common center of mass with same angular velocity. The particle does not influence their motion. The equations of motion are non-dimensionalized by the following choice of units: the mass unit MU is the sum of the two primaries masses; the length unit LU is the distance between primaries; the time unit TU is chosen such that the non-dimensional period of primaries orbit around their barycenter is equal to 2π . Normalization units are summarized in Tab. 2.1, where T is the dimensional orbital period of P_2 and P_1 , and R_{12} is the distance between primaries.

Table 2.1: Normalization units.

Symbol	Unit	Description
MU	Mass unit	$m_1 + m_2$
LU	Length unit	R_{12}
TU	Time unit	$T/(2\pi)$

The only free parameter of the system is the mass parameter $\mu = m_2/(m_1 + m_2)$. The dynamics can be expressed in a specific reference frame eliminating explicit dependence on time. This is the synodic or rotating frame, which is centered at barycenter and rotates with the same angular velocity of primaries circular orbits. In this frame, P_1 and P_2 are fixed on the x axis at $(-\mu, 0)$ and $(1 - \mu, 0)$, respectively (see Fig. 2.1).

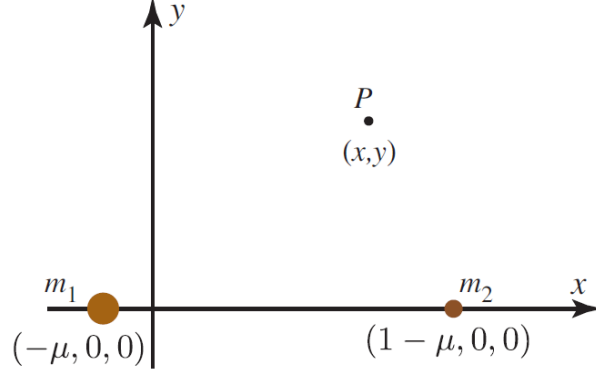


Figure 2.1: Synodic coordinate frame [21].

The planar motion of P expressed in the synodic frame is described by the following system of differential equations [2]

$$\begin{cases} \ddot{x} - 2\dot{y} = \Omega_x, \\ \ddot{y} + 2\dot{x} = \Omega_y, \end{cases} \quad (2.1)$$

where Ω is the potential function defined as

$$\Omega(x, y) = \frac{1}{2}(x^2 + y^2) + \frac{1 - \mu}{r_1} + \frac{\mu}{r_2} + \frac{1}{2}\mu(1 - \mu). \quad (2.2)$$

$r_1 = \sqrt{(x + \mu)^2 + y^2}$ and $r_2 = \sqrt{(x + \mu - 1)^2 + y^2}$ represent the distances of point P from m_1 and m_2 , respectively. Subscripts in Eq. (2.1) indicate the partial derivative of Ω with respect to the variables x and y . The CR3BP written in the synodic frame is an Hamiltonian and autonomous system, therefore it has an energy integral of motion called Jacobi constant, which reads [2]

$$J_C(x, y, \dot{x}, \dot{y}) = 2\Omega(x, y) - (\dot{x}^2 + \dot{y}^2). \quad (2.3)$$

The measurement of particle's position and velocity determines its energy. Once ICs are given, the Jacobi integral defines allowed and forbidden regions of motion for the third particle, bounded by zero velocity or Hill's curves. Each solution of Eq. (2.1) always lies on an energy surface

$$\mathcal{J}(C) = \{(x, y, \dot{x}, \dot{y}) \in \mathbb{R}^4 | J_C(x, y, \dot{x}, \dot{y}) = C\} \quad (2.4)$$

for a given energy level C . The projection of the manifold $\mathcal{J}(C)$ onto the (x, y) subspace

is called Hill's region, which marks the area where P motion is always confined. The boundary of a Hill's region is referred as zero-velocity curve [2].

The CR3BP has five equilibrium points, also called Lagrangian or libration points, which are critical points of the potential function $\Omega(x, y)$ [21]. They are stationary points and are found through

$$\nabla\Omega(x, y) = 0. \quad (2.5)$$

Three of them (L_1 , L_2 and L_3) are collinear on the x -axis, while the remaining two (L_4 and L_5) are called equilateral points (see Fig. 2.2).

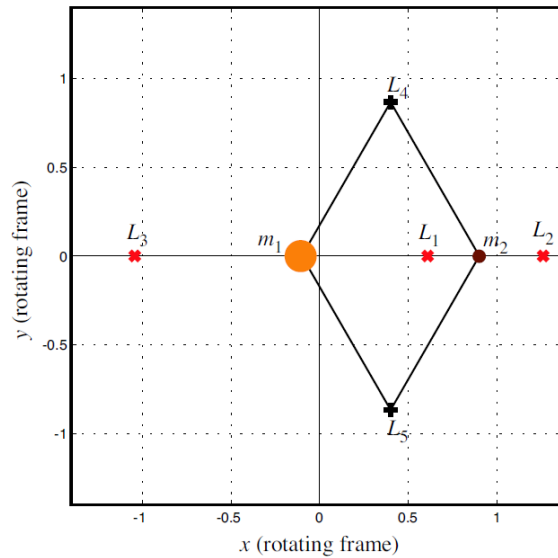


Figure 2.2: Equilibrium points of the CR3BP in the synodic frame for $\mu = 0.3$ [21].

Depending on the motion of primaries around their barycenter, the CR3BP can be considered representative of the real dynamics only in first approximation. For instance, the eccentricity of primaries orbit in the Sun–Mars system is small but not negligible ($e_p \simeq 0.09$, see Tab. 5.2). Thus, the ER3BP better describes the dynamics of a third body when the eccentricity of the primaries is not negligible.

2.1.1. Invariant manifolds

Invariant manifolds about the collinear libration points in the CR3BP supply a framework to understand the flow structure from a geometric viewpoint. Invariant manifold tubes associated with periodic orbits around Lagrangian points provide conduits for the transport from a region of the space to another one. These conduits together with the Poincaré sections can be exploited to construct spacecraft trajectories with prescribed

itineraries [21]. Collinear libration points L_i are of center-saddle type. Thus, for some range of energies C , there exist a family of periodic orbits $\gamma_i(C)$, called Lyapunov orbits, emanating from L_i . For fixed C , each periodic orbit γ_i possesses its invariant manifolds [2]. The set of phase space points from which the trajectory converges to the periodic orbit in forward time is called stable manifold $W^s(\gamma_i)$. The unstable manifold $W^u(\gamma_i)$ is the set of points from which the trajectory converges to γ_i in backward time. Trajectories starting inside the stable manifold make a transfer from one lobe of the Hill's region to the other one or to the exterior region when the dynamics is propagated forward [2]. The same happens for the unstable manifold but in backward time (see Fig. 2.3).

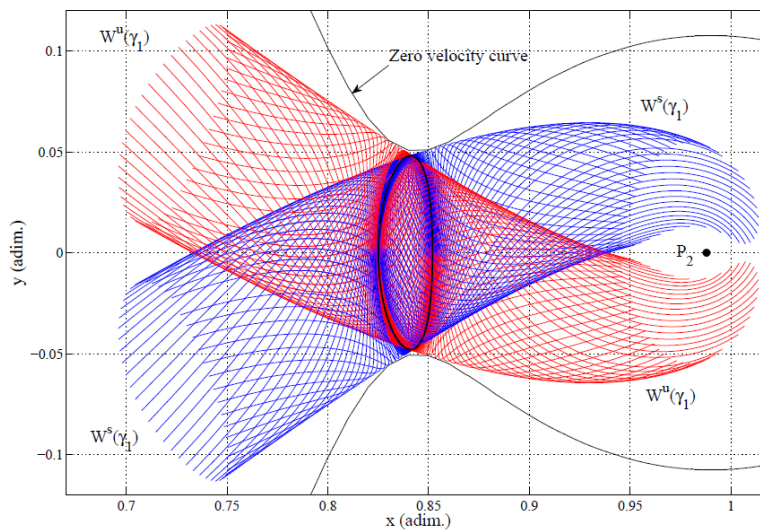


Figure 2.3: Invariant manifolds of a Lyapunov orbit about L_1 for a given energy [2].

Computation of invariant manifolds

Computational methods for determining the CR3BP invariant manifolds are well developed [21]. They are based on the linear approximation of the dynamics about an equilibrium point. In order to generate the stable or unstable manifold, one first needs to compute the periodic orbit. Differential correction is one of the available techniques. It is an iterative process which, starting from an initial state \mathbf{x}_0 , makes slight adjustments so that the adjusted trajectory will end up to a target final state. The objective is to produce ICs belonging to a periodic orbit. Local approximations of stable and unstable manifolds are obtained from eigenvectors of the monodromy matrix associated to the periodic orbit retrieved with differential correction. The monodromy matrix represents the state transition matrix (STM) (see Section 4.2) over one period of the orbit. The method to compute invariant manifolds is the following [5]:

1. For each point \mathbf{x}_0 on the periodic orbit, the monodromy matrix and its eigenvectors are computed. The normalized stable eigenvector is denoted by $\mathbf{v}_s(\mathbf{x}_0)$ and the unstable one by $\mathbf{v}_u(\mathbf{x}_0)$.
2. Then, let

$$\begin{cases} \mathbf{x}^{s\pm}(\mathbf{x}_0) = \mathbf{x}_0 \pm \alpha \mathbf{v}_s(\mathbf{x}_0), \\ \mathbf{x}^{u\pm}(\mathbf{x}_0) = \mathbf{x}_0 \pm \alpha \mathbf{v}_u(\mathbf{x}_0), \end{cases} \quad (2.6)$$

be the initial guesses for the stable and unstable manifolds. α should be small enough to guarantee validity of linear approximation, but not too small to keep a reasonable time for convergence or escape. A value of α bounded between 10^{-4} and 10^{-6} is typically a good guess [37].

3. Finally, the unstable vector $\mathbf{x}^{u\pm}(\mathbf{x}_0)$ is integrated forward in time, using both α and $-\alpha$ to generate the two branches of unstable manifold $W^{u\pm}(\mathbf{x}_0)$. The same procedure applies backward in time for the stable vector to get $W^{s\pm}(\mathbf{x}_0)$. This process is called globalization of stable and unstable manifolds [21].

Invariant manifold tubes are generated by the iteration of this steps for a number of points \mathbf{x}_0 on the periodic orbit.

Trajectories with prescribed itineraries

Invariant manifolds can be used to find trajectories with prescribed itineraries exploiting the intersections of globalized manifolds with the Poincaré sections U_i as shown in Fig. 2.4 [21].

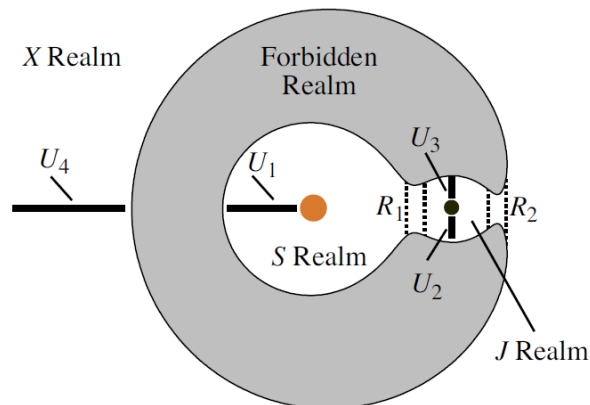


Figure 2.4: The four Poincaré sections U_i in the Sun–Jupiter system [21].

U_i are placed at strategic locations, allowing to intersect stable and unstable manifolds associated to specific periodic orbits. For instance, U_3 is chosen to intersect both the stable

manifold of L_1 periodic orbit and the unstable manifold of L_2 one. A possible strategy to construct a trajectory with a defined itinerary is to connect stable and unstable manifolds of L_1 and L_2 periodic orbits. In Fig. 2.5, the invariant manifolds projection onto the configuration space in the Sun–Jupiter (S–J) system is shown.

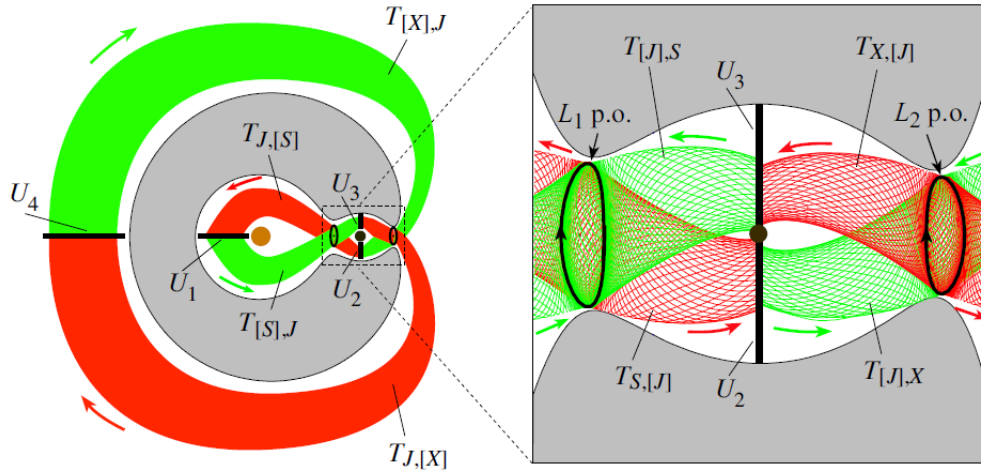


Figure 2.5: Position space projection of the L_1 and L_2 periodic orbit manifold tubes [21].

Consider the J realm and suppose to construct a trajectory with itinerary $(X, [J], S)$. This means that particle will flow from the X realm to the Sun one, passing from the Jupiter realm (see Fig. 2.4). ICs that generate this trajectory can be found on the U_3 Poincaré section. Referring to Figs. 2.5 and 2.6, ICs in the $(X, [J], S)$ region stay within the $T_{[J],S}$ tube if integrated forward, while remain inside $T_{X,[J]}$ if integrated backward.

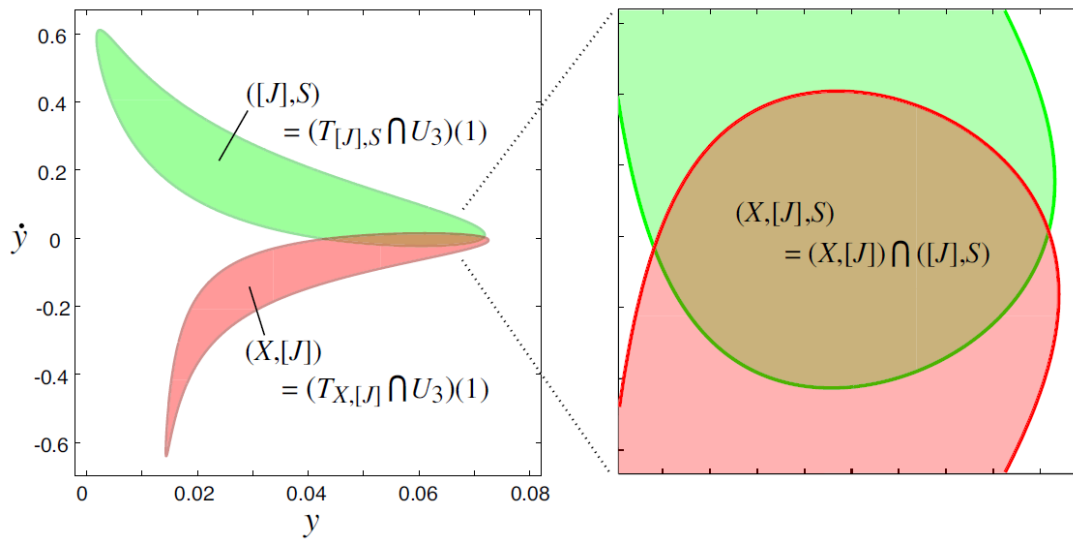


Figure 2.6: An itinerary region $(X, [J], S)$ [21].

This approach can also be exploited for the design of low-energy interplanetary transfers. Invariant manifolds of two different Sun–Planet systems can be coupled to generate ballistic capture interplanetary trajectories [37].

2.2. Planar elliptic restricted three-body problem

The ER3BP is a natural generalization of the CR3BP in which primaries move on elliptical orbits around their barycenter [11, 19, 36]. Similarly to the CR3BP, the dynamics can be expressed in a non-uniformly rotating, barycentric, non-dimensional frame where P_1 and P_2 have fixed positions (Fig. 2.1). The main difference with the CR3BP is that the coordinate frame isotropically pulsates along P_1 – P_2 direction. Non-dimensionalization strategy follows that of the circular problem, but the distance between primaries R_{12} is not constant. It is given by the solution of the two body problem relative to P_1 – P_2 motion

$$R_{12}(f) = \frac{a_p(1 - e_p^2)}{1 + e_p \cos(f)}, \quad (2.7)$$

where a_p and e_p are respectively the semi-major axis and eccentricity of P_1 – P_2 system. $f(t)$ denotes the true anomaly of the system (Fig. 2.7). True anomaly is designated to be the independent variable of the system and covers the role of time. The dependence of true anomaly on time reads [36]

$$\frac{df}{dt} = \frac{(1 + e_p \cos f)^2}{(1 - e_p^2)^{\frac{3}{2}}}. \quad (2.8)$$

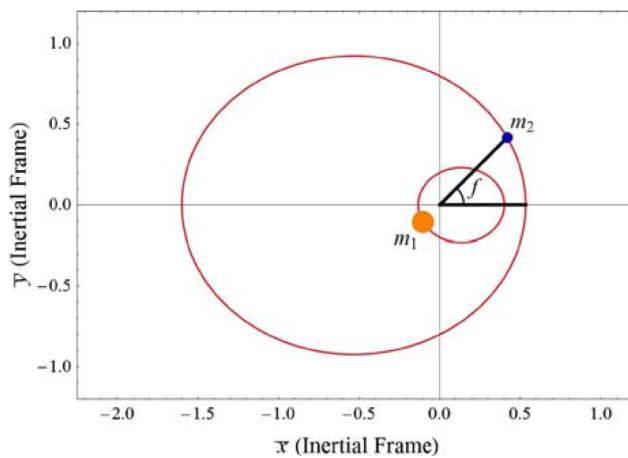


Figure 2.7: Elliptical orbits of primaries in the ER3BP with respect to an inertial barycentric frame for $e_p = 0.5$, $\mu = 0.2$ [11].

Assuming planar motion of the third particle, the ER3BP dynamics reads

$$\begin{cases} x'' - 2y' = \omega_x, \\ y'' + 2x' = \omega_y, \end{cases} \quad (2.9)$$

where $(\cdot)''$ and $(\cdot)'$ indicate differentiation with respect to f , while ω_x and ω_y express the partial derivatives along x and y , respectively, of the ER3BP potential function [19]

$$\omega(x, y, f) = \frac{\Omega(x, y)}{1 + e_p \cos(f)}, \quad (2.10)$$

where Ω is the potential function of CR3BP. Note that when $e_p = 0$, the true anomaly coincides with time. In this case, Eq. (2.9) reduces to the equations of motion of the circular problem. Unlike the CR3BP, the dependence on f makes the system non-autonomous, hence the dynamics has no more a constant integral of motion but it depends on f . The anomaly-dependent integral of motion of the planar ER3BP reads

$$J_E(x, y, x', y', f) = 2\omega - (x'^2 + y'^2) - 2e_p \int_{f_0}^f \frac{\Omega \sin(\tilde{f})}{(e_p \cos(\tilde{f}))^2} d\tilde{f}. \quad (2.11)$$

Setting $e_p = 0$ the Jacobi integral of circular problem in Eq. (2.3) is retrieved. Since J_E is anomaly-dependent, allowed and forbidden regions of motion for a given energy level are no more fixed like in the CR3BP. In particular, pulsating Hill's curves appear and vary according P_1 - P_2 motion. Fig. 2.8 shows the Hill's curves associated with the same initial state, but with different initial anomaly f_0 . Like the CR3BP, also the elliptic problem has five equilibrium points as shown in Fig. 2.2. However, their real distance from P_1 and P_2 pulsates according to the primaries position.

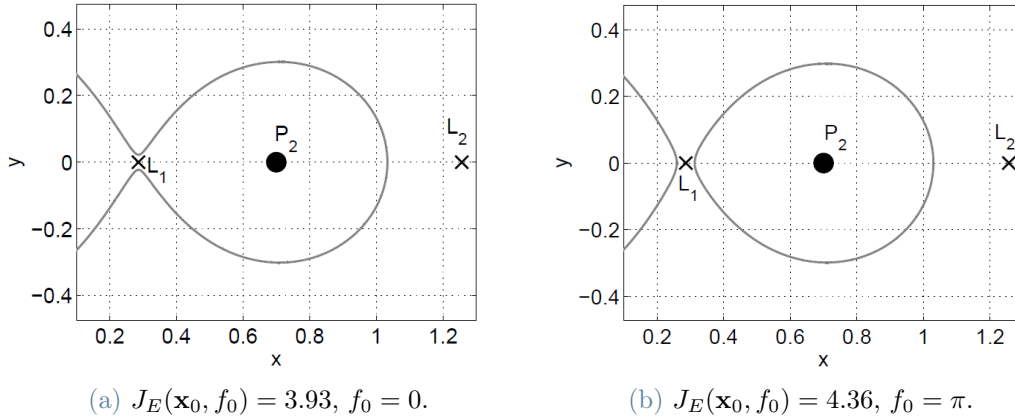


Figure 2.8: Regions of motion associated to $\mathbf{x}_0 = [1, 0, 0.25, 0.3]$ ($\mu = 0.3, e_p = 0.05$) [19].

3 | Ballistic capture

The design of ballistic capture orbits is not trivial, and there is not a systematic way to derive arrival orbits matching exactly mission constraints. Design can be performed by following two different strategies. The first one analyzes the phase space structure around the collinear libration points in the CR3BP. As previously mentioned in Section 2.1.1, invariant manifolds of periodic orbits around L_1 or L_2 separate regions where the flow has different attitude, acting as dynamics separatrices [21]. Ballistic trajectories can be designed from the globalization of invariant manifolds together with Poincaré sections. An advantage of this method is that it gives insight into the dynamics of the capture. Drawbacks are the inability to control orbital elements of the final capture orbit, and that the method is only applicable in the CR3BP. Concepts of equilibrium points, periodic orbits and their invariant manifolds disappear when the fourth-body perturbation or orbital eccentricities of the primaries are taken into account. In the latter case LCSs-like approaches can be exploited, as will be discussed in Chapter 4. LCSs can be considered a generalization of invariant manifolds for time-dependent dynamical systems.

The other design strategy exploits the concepts of stable sets and WSBs. Stability definitions can be extended to models including primaries eccentricities and perturbations. The method relies on sampling the phase space around the target primary and integrating a large number of orbits. The basic drawback is the brute-force nature of this approach, which is in general computationally more intensive compared with invariant manifolds computation. Moreover, stable sets can be used as black-box tools and do not require intricate knowledge of the dynamics about the target. Stable sets contain less information from a dynamic perspective compared with invariant manifolds.

3.1. Orbits classification

The key point of ballistic capture orbits design through stable sets manipulation is to find sets of ICs in a phase space region around the target whose orbits satisfy specific conditions [19, 24]. The objective is to find trajectories with a peculiar behaviour when the dynamics is integrated forward or backward in time. This is achieved applying spatial

stability definitions while integrating a set of ICs. In this section, a generalized notion of stability in three-dimensions is presented, opening up to the possibility to implement the strategy in high-fidelity astrodynamical models [24], but also in less complicated ones such as the CR3BP and ER3BP [19]. Spatial stability conditions are formulated in a target-centered inertial frame that tracks the true number of revolutions of a third particle around the target. This prevents discrepancies in the number of revolutions between the inertial and rotating frame. The method is able to categorize ICs in a certain region in proximity of the target into different subsets according to the orbits they generate.

In three-dimensions, an IC is specified by six orbital elements, or equivalently by its position (\mathbf{r}_0) and velocity (\mathbf{v}_0) in a target-centered inertial frame. Once the position is fixed, velocity is computed assuming that the particle starts its motion at periapsis of a Keplerian orbit around the target with fixed osculating eccentricity e . It has been shown that values of $e \in [0.9, 1)$ are appropriate to support ballistic capture [19]. Particle stability can be inferred by studying intersections of its trajectory with an intersection plane spanned by \mathbf{r}_0 and $\mathbf{h}_0 = \mathbf{r}_0 \times \mathbf{v}_0$. Geometric and energetic conditions that rule revolution, escape, or impact of the particle are presented in three following remark points [24]. The following conditions in the remarks can be applied for different orientations of the target-centered inertial frame.

Remark 1 (Revolution). *The particle performs a complete revolution around the target at time t_r if the following conditions are simultaneously satisfied,*

$$\begin{cases} \mathbf{r}^{(k)}(t_r) \cdot (\mathbf{h}_0 \times \mathbf{r}_0) = 0, \\ \mathbf{r}^{(k)}(t_r) \cdot \mathbf{r}_0 > 0, \\ (\mathbf{v}^{(k)}(t_r) \cdot \mathbf{v}_0)(\mathbf{v}^{(k-1)} \cdot \mathbf{v}_0) > 0, \end{cases} \quad (3.1)$$

where k counts the number of intersections.

First condition in Eq. (3.1) assures that the particle returns to the intersection plane; the second one avoids counting semi-revolutions, restricting the analysis to the semi-plane of interest; the third one discards multiple intersections associated to incomplete revolutions, as shown in Fig. 3.1.

Remark 2 (Escape). *The particle escapes from the target at time t_e if the following conditions are satisfied,*

$$\begin{cases} H(t_e) > 0, \\ r(t_e) > R_s, \end{cases} \quad (3.2)$$

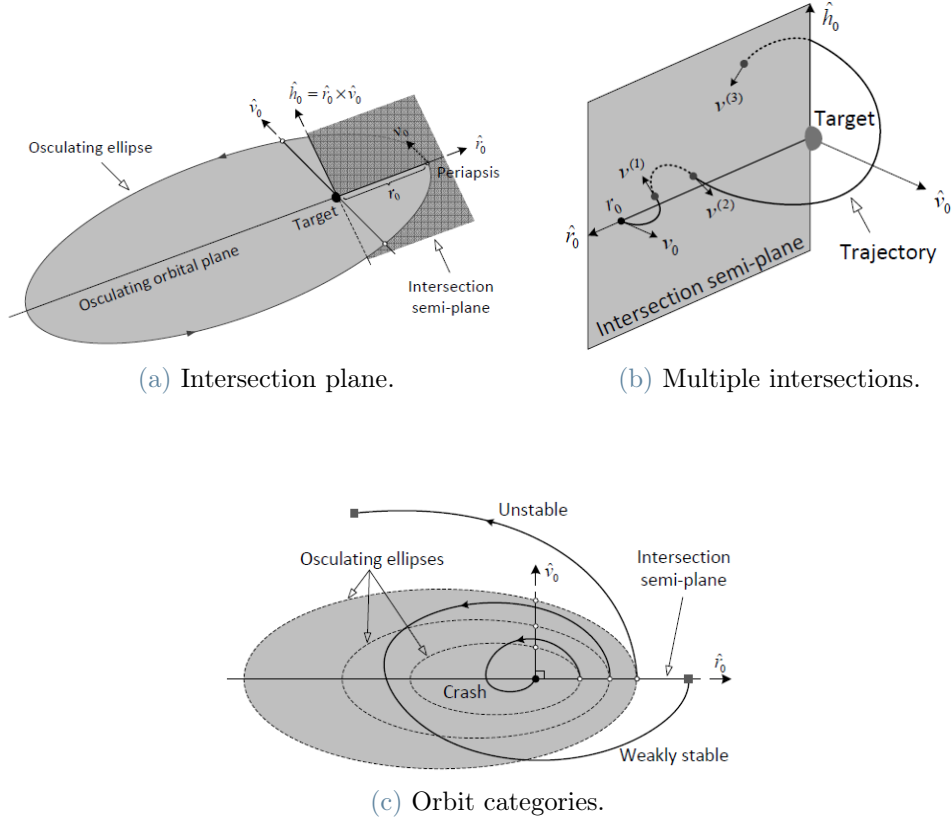


Figure 3.1: Intersection plane and orbit categories [24].

where $H(t_e)$ is the Kepler energy of the particle with respect to the target and R_s is the radius of the target sphere of influence.

The Kepler energy H of the particle is not constant due to third-body perturbations. Its sign suggests which body dominates over the particle trajectory [23].

Remark 3 (Impact). *The particle impacts with the target at time t_i if*

$$r(t_i) < R_{eq}, \quad (3.3)$$

where R_{eq} is the target mean equatorial radius.

Consider a phase space region around the target primary sampled with ICs. Starting from the periapsis condition, each initial state is propagated. According to the global behavior of generated orbits, it is possible to divide ICs into four non-intersecting subsets for different values of n . The stability number n defines the number of complete revolutions of the particle around the target. ICs are integrated for a given amount of time, sufficiently long to properly classify the orbits, and then split into subsets $(\mathcal{W}_n, \mathcal{X}_n, \mathcal{K}_n, \mathcal{D}_n)$.

Classification sets are defined as follows [23]:

Weakly stable set \mathcal{W}_n contains ICs whose orbits perform n complete revolutions around the target.

Unstable set \mathcal{X}_n contains ICs whose orbits escape from the target after performing $n-1$ complete revolutions.

Crash set \mathcal{K}_n contains ICs whose orbits impact with the target after performing $n-1$ complete revolutions.

Acrobatic set \mathcal{D}_n contains ICs whose orbits perform $n - 1$ complete revolutions around the target and then do not satisfy none of the previous conditions within the given time span.

Fig. 3.2 displays different classes of orbits with $n = 1$ about Mercury.

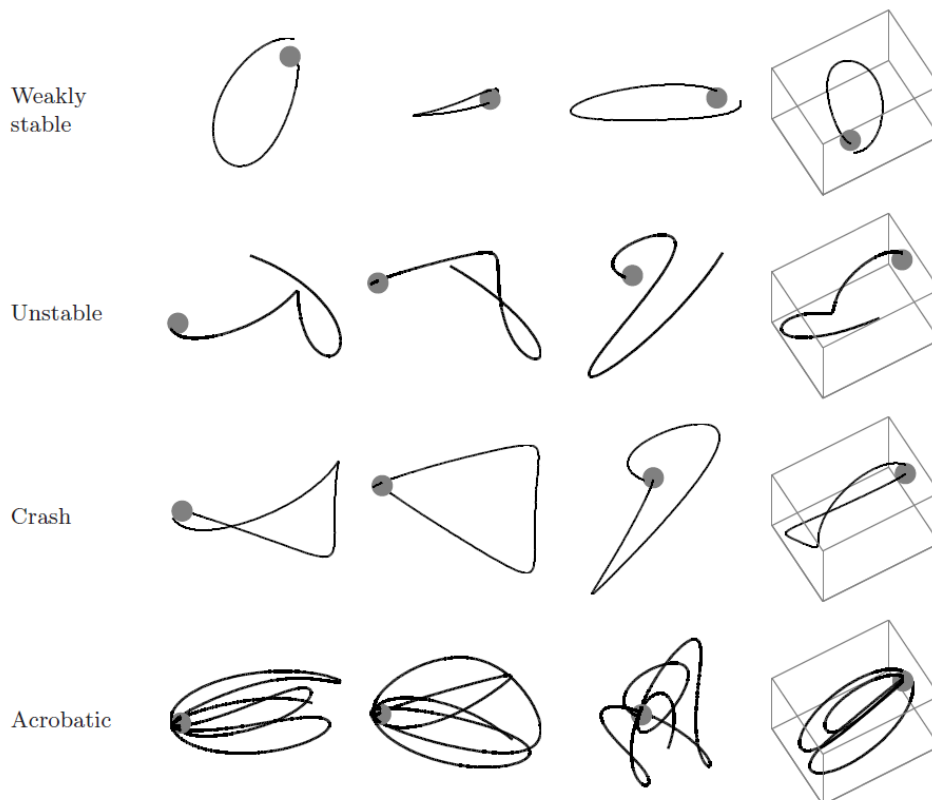


Figure 3.2: Sample orbits around Mercury, $n = 1$ [24].

3.2. Design of ballistic capture orbits

The value of n can be any non-zero integer number. When a negative n is considered, the stability conditions introduced before are applied in backward time. In this case, for $n = -1$, the sets \mathcal{W}_{-1} , \mathcal{X}_{-1} , \mathcal{K}_{-1} and \mathcal{D}_{-1} are generated. If \mathbb{I} is the set of all ICs, the following relations hold

$$\mathbb{I} = \mathcal{W}_1 \cup \mathcal{X}_1 \cup \mathcal{K}_1 \cup \mathcal{D}_1 = \mathcal{W}_{-1} \cup \mathcal{X}_{-1} \cup \mathcal{K}_{-1} \cup \mathcal{D}_{-1}, \quad (3.4)$$

$$\mathcal{W}_{n-1} = \mathcal{W}_n \cup \mathcal{X}_n \cup \mathcal{K}_n \cup \mathcal{D}_n. \quad (3.5)$$

Practical ballistic capture orbits are generated by ICs which are in the capture set obtained through

$$\mathcal{C}_{-1}^n = \mathcal{X}_{-1} \cap \mathcal{W}_n. \quad (3.6)$$

Conditions in \mathcal{C}_{-1}^n generate orbits that approach the target coming from outside its sphere of influence and perform n revolutions around it without escaping or crashing (Fig. 3.3).

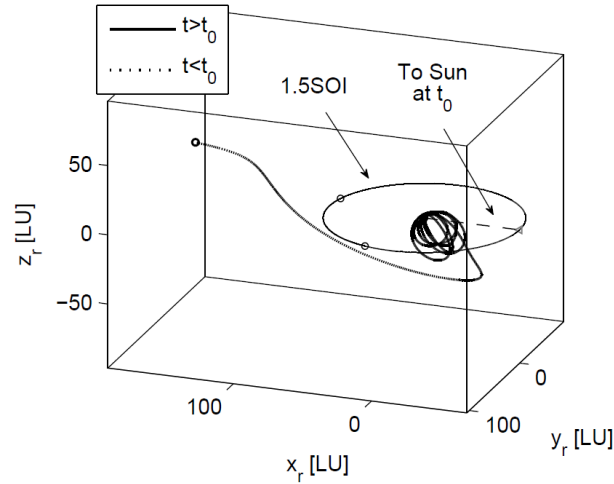
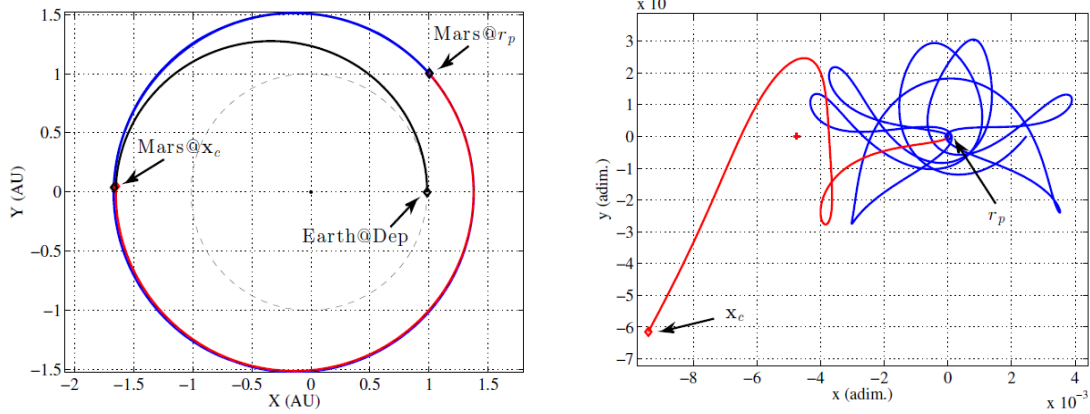


Figure 3.3: Sample orbit about Mercury of \mathcal{C}_{-1}^6 capture set [23].

An Earth–Mars transfer strategy with ballistic capture is studied in [36]. Stability definitions and classification of orbits are slightly different from the ones presented in this chapter, and are described in [19]. The reference dynamical model is the planar ER3BP. The purpose is to construct a transfer from Earth to Mars at the point \mathbf{x}_c , from which to begin a ballistic capture orbit that will go naturally at a periapsis distance r_p from Mars. \mathbf{x}_c is obtained by integrating an IC in \mathcal{C}_{-1}^n in backward time. A sample solution is given in Fig. 3.4.



(a) Sun-centered frame (the black orbit is the orbit that targets \mathbf{x}_c departing from the Earth; the red orbit is the capture orbit; the blue orbit is the post-capture orbit).

(b) The capture orbit (red) and the post-capture orbit (blue) in the rotating Mars-centered frame.

Figure 3.4: Sample solution of an Earth–Mars transfer in \mathcal{C}_{-1}^6 [36].

4 | Lagrangian coherent structures

4.1. Definition and properties

In autonomous dynamical systems, like the CR3BP, invariant manifolds theory applied to fixed points and periodic orbits is very useful in determining the qualitative properties of groups of trajectories, as seen in Section 2.1.1. This approach allows to predict the evolution of sets of ICs avoiding their explicit integration. However, concepts of fixed points, stable and unstable manifolds are lost for non-autonomous dynamical systems with arbitrary time dependence (e.g. ER3BP, n -body problem) or for flows only defined over a finite time interval. While Poincaré maps and invariant manifolds concepts are less effective in this context, families of hyperbolic material lines continue to organize flow transport mechanisms. LCSs can be considered as a generalization of invariant manifolds in the time-dependent case, underlying the key aspects of material transport for a generic flow [14]. They are time-evolving structures in the phase space of a generic dynamical system which form the skeleton of observed flow patterns.

The LCS acronym was coined by G. Haller and G. Yuan in 2000 [13]. The aim of the researchers was to uncover special structures, a robust skeleton of material surfaces, that give an idea of the evolution of the flow after a certain time interval. The word Lagrangian reflects the fact that these structures evolve with the fluid particles, as a material surface does. LCSs are expected to have two key properties [16]:

- An LCS should be a material surface $\mathcal{M}(t)$, which is a codimension-one invariant surface in the extended phase space of a dynamical system (Fig. 4.1). An invariant surface is any set of points which are mapped into other points of the same set when advected by the flow map. An LCS should be a material surface for two reasons. Firstly because its dimension should be high enough to have visible impact and act as transport barrier. Secondly because an LCS must move with the flow.
- An LCS should exhibit locally the strongest repulsion, attraction, or shearing in the flow over a finite time interval. The strongest repelling or attracting material surfaces are called hyperbolic LCSs (see Fig. 4.2).

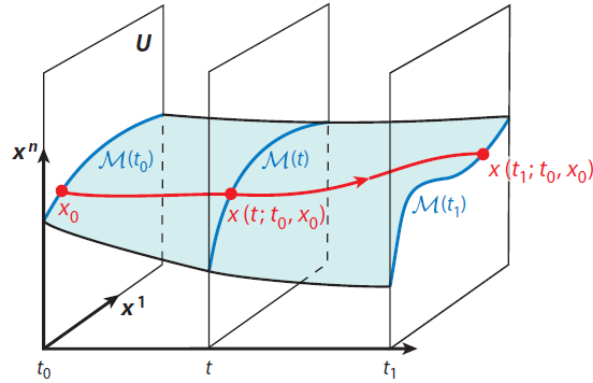


Figure 4.1: Material surface evolution in the extended phase space [14].

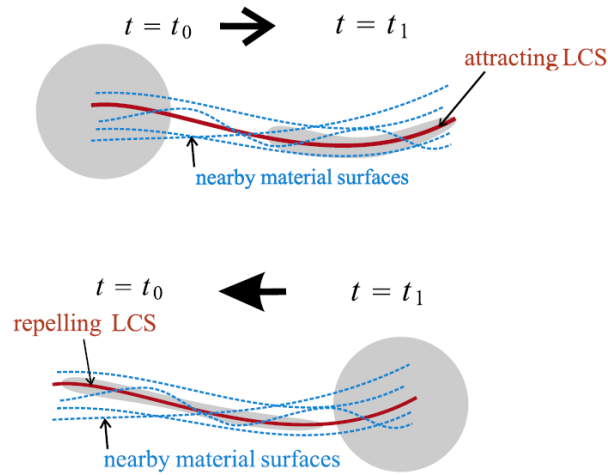


Figure 4.2: Hyperbolic LCSs [16].

For years LCSs have not had a mathematical definition. Initially they have been defined as ridges of the finite-time Lyapunov exponent (FTLE) field [15], but simple counterexamples revealed some problems with that identification. Despite that, FTLE remains a useful and fast visual tool to identify patterns in the flow also in complex dynamical systems. A more mathematical and rigorous formulation takes the name of variational theory [16]. This theory covers the inconsistencies of FTLE approach, giving sufficient and necessary conditions for the existence of hyperbolic LCSs. More recently, new techniques to detect phase space structures for a generic system have been developed. One of them is the LDs approach [27]. This tool provides a characterization of dynamical systems, underlying geometrical structures in the phase space that organize particles by regions corresponding to different types of trajectories. Being heuristic, FTLE and LD methods could underline false positives or false negatives, nevertheless they are a useful and fast tool for qualitative dynamics description. LCSs computation from variational theory requires additional effort to be implemented, but eliminates inconsistencies.

4.2. Variational equations

The equations of motion of a generic dynamical system can be expressed as [33]

$$\begin{cases} \dot{\mathbf{x}}(t) = \mathbf{f}(\mathbf{x}(t), t), \\ \mathbf{x}(t_0) = \mathbf{x}_0, \\ \mathbf{x}(t) \in \Omega \subseteq \mathbb{R}^n, \\ t \in I = [\alpha, \beta], \end{cases} \quad (4.1)$$

where t is the independent variable representing time, while $\mathbf{x}(t)$ is the state vector. The vector field \mathbf{f} is also called velocity map. The solution of Eq. (4.1) can be viewed, alternatively, as a flow map $\phi_{t_0}^t$ applied to the initial condition \mathbf{x}_0 ,

$$\phi_{t_0}^t(\mathbf{x}_0) = \mathbf{x}(\mathbf{x}_0, t_0; t). \quad (4.2)$$

A perturbed initial condition $\mathbf{x}_0 + \delta\mathbf{x}_0$ will generate a perturbed trajectory $\mathbf{x} + \delta\mathbf{x}$, whose perturbation $\delta\mathbf{x}$ can be estimated from a linearization of the flow map in \mathbf{x}_0 . Assuming flow map differentiability,

$$\delta\mathbf{x} = \frac{\partial \phi_{t_0}^t}{\partial \mathbf{x}_0}(\mathbf{x}_0, t_0; t) \delta\mathbf{x}_0 = \mathbf{\Phi}(\mathbf{x}_0, t_0; t) \delta\mathbf{x}_0, \quad (4.3)$$

where $\mathbf{\Phi}$ is denoted as STM and $\mathbf{\Phi}(\mathbf{x}_0, t_0; t) = \mathbf{I}_n$. \mathbf{I}_n is the n -dimensional identity matrix. The Jacobian of the flow is defined as $\mathbf{A}(\mathbf{x}, t) = \frac{\partial \mathbf{f}(\mathbf{x}, t)}{\partial \mathbf{x}}$. At this point one can write the following system [33]

$$\begin{cases} \dot{\mathbf{\Phi}} = \mathbf{A}(\mathbf{x}, t) \mathbf{\Phi}, \\ \mathbf{\Phi}(\mathbf{x}_0, t_0; t) = \mathbf{I}. \end{cases} \quad (4.4)$$

Eqs. (4.1) and (4.4) together make up the variational equations of the dynamical system, which is $(n + n^2)$ -dimensional. The variational equations can be propagated to compute the STM of the flow at a given time instant. This is essential for the LCSs extraction strategies presented in the following sections.

4.3. Finite-time Lyapunov exponent

The FTLE approach represents one of the first developed strategies to locate LCSs in the phase space of a dynamical system with arbitrary time dependence [15, 17, 35]. A repelling LCS should appear as a local maximizing curve (ridge) of the FTLE field computed over a grid of initial states. Equivalently, an attracting LCS should be a ridge of the FTLE field obtained propagating ICs in backward time. For autonomous systems, FTLE fields contour levels can approximate stable and unstable manifolds of fixed points and periodic orbits.

The FTLE is essentially a finite time average of the maximum separation rate for two infinitesimally close ICs advected by the flow map. It measures how much particles separate after a given interval of time. Therefore, from a mathematical standpoint, FTLE can be derived from the evolution of a perturbed point after a finite time interval T . Recalling Eq. (4.3), the magnitude squared of the linearized evolution of the infinitesimal perturbation after a time T can be written as

$$\|\delta\mathbf{x}(t_0 + T)\|^2 = \delta\mathbf{x}_0^T \Phi^T \Phi \delta\mathbf{x}_0 = \delta\mathbf{x}_0^T \Delta \delta\mathbf{x}_0, \quad (4.5)$$

where Δ is the finite-time Cauchy-Green (CG) deformation tensor, which is function of t_0 , T , and \mathbf{x}_0 . It is symmetric and positive definite. Maximum stretching occurs when $\delta\mathbf{x}_0$ is aligned with the eigenvector associated with the maximum eigenvalue of Δ , λ_{max} . Thus, the FTLE definition reads

$$\sigma_{t_0}^T(\mathbf{x}_0) = \frac{1}{|T|} \ln \sqrt{\lambda_{max}} \quad (4.6)$$

and represents the finite-time Lyapunov exponent with an integration time T associated to the initial state \mathbf{x}_0 inside the domain of interest. Integration time T can be either positive or negative. In particular, forward-time integration ($T > 0$) locates repelling LCSs (e.g. stable manifolds in autonomous systems) and backward-time integration ($T < 0$) locates attracting LCSs (e.g. unstable manifolds in autonomous systems). In Fig. 4.3 ridges of the FTLE field computed in both time directions for a vortex behind a cylinder are displayed.

Consider a hyperbolic fixed point and its stable and unstable manifolds as those shown in Fig. 4.4. The two points on either side of the stable manifold will diverge after a sufficient amount of time. Therefore, high FTLE values can be expected along the stable manifold and, roughly speaking, as T increases more of the LCSs becomes resolved.

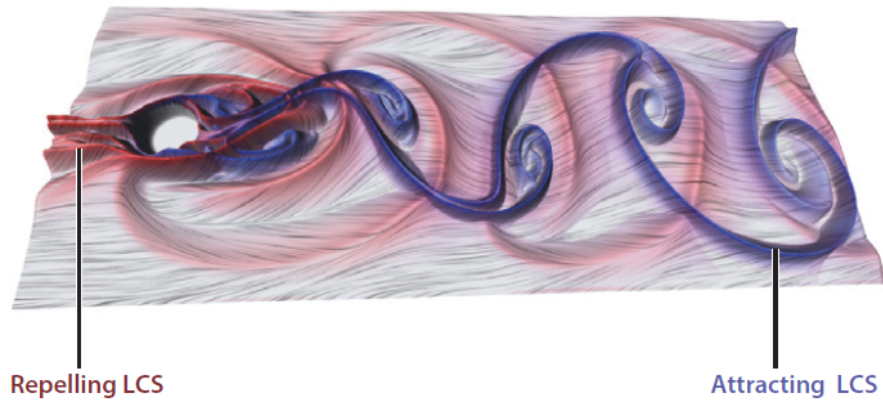


Figure 4.3: Repelling and attracting LCS candidates as ridges of forward and backward FTLE field for a vortex behind a cylinder [14].

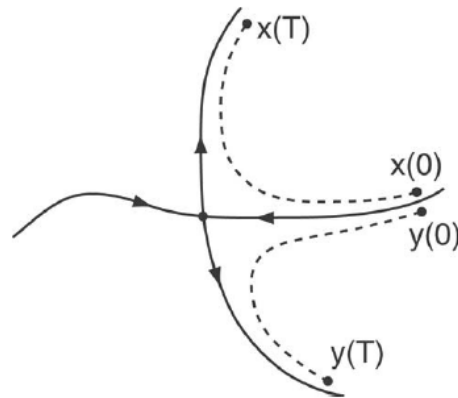


Figure 4.4: Two points on opposite sides of a stable manifold will diverge after a sufficient amount of time [35].

The issue related with FTLE is that, being a heuristic approach, it does not provide sufficient and necessary conditions for LCS existence that are supported by mathematical theorems. FTLE ridges can produce false positives in LCSs detection and not every LCS is related to an FTLE ridge, even in simple two-dimensional steady flows [16]. FTLE theory may give wrong results because, as opposed to variational theory (see Section 4.4), the procedure ignores the direction of the eigenvector associated to λ_{max} . Nevertheless it remains a valid fast preliminary tool to locate coherent structures in non-autonomous systems.

A generic dynamical system expressed in its variational form is written as

$$\begin{cases} \dot{\mathbf{x}}(t) = \mathbf{f}(\mathbf{x}(t), t), \\ \mathbf{x}(t_0) = \mathbf{x}_0, \\ \dot{\Phi} = \mathbf{A}(\mathbf{x}, t) \Phi, \\ \Phi(t_0; t_0, \mathbf{x}_0) = \mathbf{I}, \\ \mathbf{x}(t) \in \Omega \subseteq \mathbb{R}^n, \\ t \in I = [\alpha, \beta], \end{cases} \quad (4.7)$$

with $\mathbf{x}_0 \in \Omega \subseteq \mathbb{R}^n$ being an arbitrary point in the domain Ω and $[t_0, t_0 + T] \subset [\alpha, \beta]$ the finite-time integration interval. Once $\Phi(t_0 + T; t_0, \mathbf{x}_0)$ is obtained, the CG strain tensor is computed together with its greatest eigenvalue λ_n , from which FTLE can be easily computed through Eq. (4.6). Algorithm 1 generates the FTLE field for a grid of ICs in the subspace of interest of a dynamical system.

Algorithm 1 FTLE visualization algorithm

- 1: $G \subset \Omega$ is the grid of initial conditions in the phase space
 - 2: $[t_0, t_0 + T]$ is the integration time interval
 - 3: **for** each $\mathbf{x}_0 \in G$ **do**
 - 4: Obtain Φ integrating system Eq. (4.7)
 - 5: $\Delta = \Phi^T \cdot \Phi$
 - 6: Solve the eigenvalue problem associated to Δ
 - 7: $\sigma_{t_0}^T(\mathbf{x}_0) = \frac{1}{|T|} \ln \sqrt{\lambda_n}$
 - 8: **end for**
 - 9: Plot $\sigma_{t_0}^T(\mathbf{x}_0)$, $\forall \mathbf{x}_0 \in G$, in the two-dimensional subspace of interest
-

An example of FTLE algorithm application is given. The selected problem is the double gyre, a two-dimensional non-linear dynamical system having equations of motion

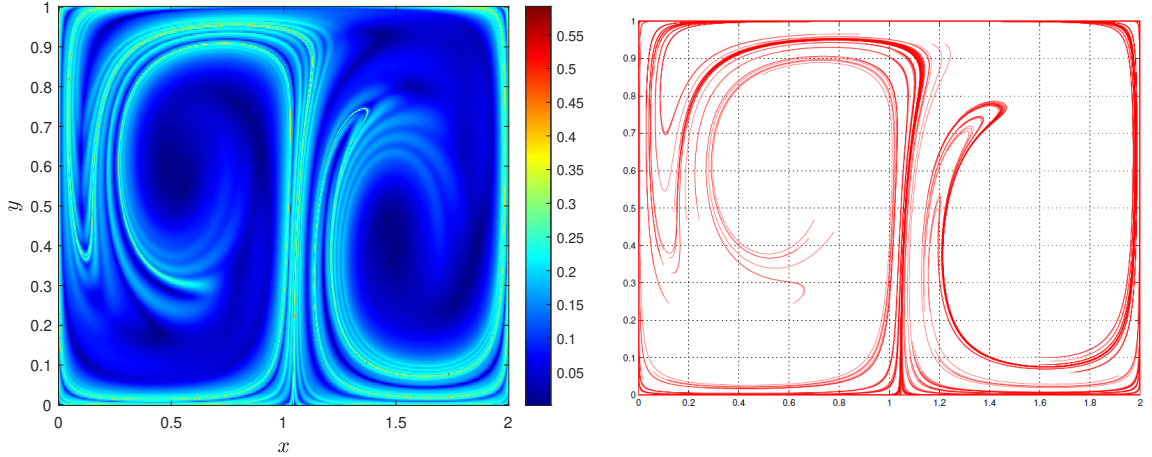
$$\begin{cases} \dot{x} = -A\pi \sin(\pi f(x, t)) \cos(\pi y), \\ \dot{y} = A\pi \cos(\pi f(x, t)) \sin(\pi y) \frac{\partial f}{\partial x}(x, t), \end{cases} \quad (4.8)$$

where

$$f(x, t) = a(t)x^2 + b(t)x, \quad a(t) = \epsilon \sin(\omega t), \quad b(t) = 1 - 2a(t), \quad (4.9)$$

with A, ϵ, ω arbitrary parameters. The chosen phase space domain is $G = [0, 2] \times [0, 1]$ with $[600 \times 300]$ grid points. The parameters used in the computation are $A = 0.1$,

$\epsilon = 0.1$, $\omega = 2\pi/10$, $t_0 = 0$ and $T = 20$. In order to validate the algorithm, a comparison with repelling LCSs computed with variational theory by the author of [33] is shown in Fig. 4.5.



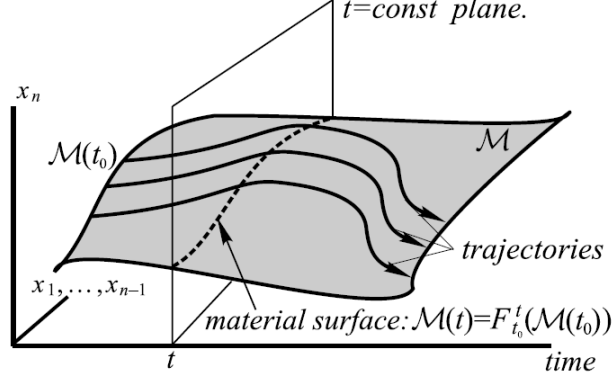
(a) FTLE field computed with Algorithm 1. (b) Repelling LCSs computed with variational theory [33].

Figure 4.5: Double gyre phase space structures.

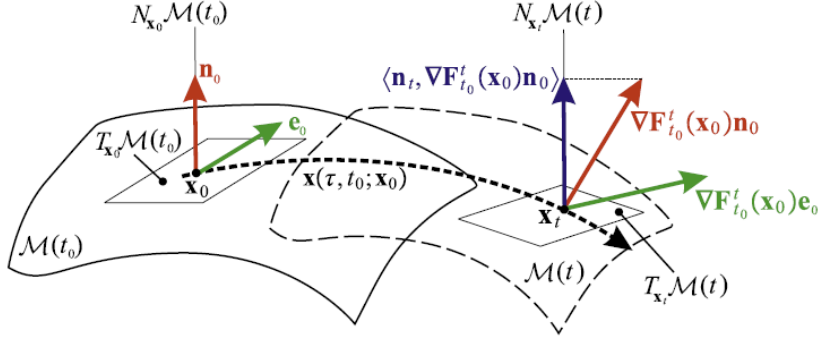
The FTLE field computed with Algorithm 1 provides good results. Lighter curves correspond to the ridges of the field, therefore to repelling LCS candidates. Ridges resemble with good approximation repelling LCSs computed with variational theory. However, as already discussed, inconsistencies of FTLE theory do not allow to classify, for a generic problem, the ridges as coherent structures.

4.4. Variational theory

A rigorous definition of LCSs has been recently provided by Haller within his variational theory [7, 16, 17]. Consider a material surface $\mathcal{M}(t_0)$ of initial conditions which is advected by the flow map into a time evolving surface $\mathcal{M}(t) = \phi_{t_0}^t \mathcal{M}(t_0)$ (see Fig. 4.6a). For each point $\mathbf{x}_0 \in \mathcal{M}(t_0)$, the evolution of the unit normal \mathbf{n}_0 to $\mathcal{M}(t_0)$ advected by linearized flow map is monitored. The normal repulsion rate $\rho_{t_0}^t(\mathbf{x}_0, \mathbf{n}_0)$ is the length of the surface-normal component of the advected vector $\nabla \phi_{t_0}^t(\mathbf{x}_0) \mathbf{n}_0$, and quantifies the normal attraction or repulsion of $\mathcal{M}(t)$, as shown in Fig. 4.6b.



(a) Material surface $\mathcal{M}(t)$ generated in the extended phase space by the flow map from $\mathcal{M}(t_0)$.



(b) Geometry of the linearized flow map along an evolving material surface $\mathcal{M}(t)$. In the picture the flow map is defined as $\mathbf{F}_{t_0}^t$.

Figure 4.6: Evolving material surface $\mathcal{M}(t)$ [16].

The normal repulsion rate can be computed in terms of the CG strain tensor as [16]

$$\rho_{t_0}^t(\mathbf{x}_0, \mathbf{n}_0) = \frac{1}{\sqrt{\mathbf{n}_0 \cdot (\Delta^{-1}(t; t_0, \mathbf{x}_0) \mathbf{n}_0)}}. \quad (4.10)$$

The repulsion ratio $\nu_{t_0}^t(\mathbf{x}_0, \mathbf{n}_0)$ is another parameter which is defined in order to assess which effect, between repulsion and shearing, is the dominant one [16],

$$\nu_{t_0}^t(\mathbf{x}_0, \mathbf{n}_0) = \min_{\substack{|\mathbf{e}_0|=1 \\ \mathbf{e}_0 \in T_{\mathbf{x}_0} \mathcal{M}(t_0)}} \frac{\rho_{t_0}^t(\mathbf{x}_0, \mathbf{n}_0)}{\sqrt{\mathbf{e}_0 \cdot (\Delta(t; t_0, \mathbf{x}_0) \mathbf{e}_0)}}. \quad (4.11)$$

If $\rho_{t_0}^t(\mathbf{x}_0, \mathbf{n}_0) > 1$, then the material surface exerts net normal repulsion on nearby fluid particles. Similarly, if $\rho_{t_0}^t(\mathbf{x}_0, \mathbf{n}_0) < 1$, $\mathcal{M}(t)$ attracts nearby elements along its normal direction. If the condition $\nu_{t_0}^t(\mathbf{x}_0, \mathbf{n}_0) > 1$ is verified, then the normal growth is higher

with respect to the tangential one. Under this condition, a repelling (attracting) LCS is a material surface $\mathcal{M}(t)$ whose net repulsion $\rho_{t_0}^t(\mathbf{x}_0, \mathbf{n}_0)$ is pointwise maximal (minimal) with respect to perturbations of \mathbf{n}_0 . Instead, a shear LCS is a material surface which maximizes net shear $\sigma_{t_0}^t(\mathbf{x}_0, \mathbf{n}_0) = \nabla \phi_{t_0}^t(\mathbf{x}_0) \mathbf{e}_0$ [14]. From a physical standpoint repelling LCSs are the core structures generating stretching and attracting LCSs act as centerpieces of folding (see Fig. 4.7). Shear LCSs delineate swirling and jet-type patterns.

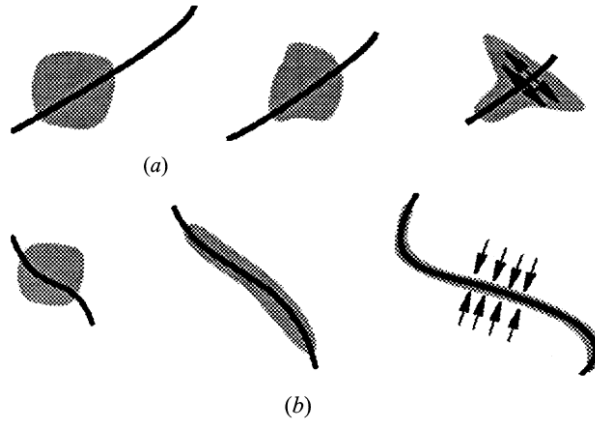


Figure 4.7: The role of coherent structures in stretching (a) and folding (b) [13].

Variational theory provides sufficient and necessary conditions for a material surface to be an hyperbolic LCS in terms of the invariants of the CG strain tensor. Conditions are summarized in Theorem 4.1 [16]. Being symmetric and positive definite, it admits n real positive eigenvalues and orthogonal real eigenvectors. The associated eigenvalue problem reads

$$\Delta(t_0 + T; t_0, \mathbf{x}_0) \boldsymbol{\xi}_i(\mathbf{x}_0) = \lambda_i(\mathbf{x}_0) \boldsymbol{\xi}_i(\mathbf{x}_0), \quad |\boldsymbol{\xi}_i(\mathbf{x}_0)| = 1, \quad i = 1, \dots, n, \quad \mathbf{x}_0 \in \mathbb{R}^n. \quad (4.12)$$

Dependence of λ_i and $\boldsymbol{\xi}_i$ on t_0 and T is suppressed for notational simplicity.

Theorem 4.1 (Repelling LCS). *Considering a compact material surface $\mathcal{M}(t) \subset U \subset \mathbb{R}^n$ over a time interval $[t_0, t_0 + T]$, it is a repelling LCS over the given time interval if and only if the following conditions are satisfied for all $\mathbf{x}_0 \in \mathcal{M}(t_0)$:*

1. $\lambda_{n-1}(t_0 + T; t_0, \mathbf{x}_0) \neq \lambda_n(t_0 + T; t_0, \mathbf{x}_0) > 1$,
2. $\boldsymbol{\xi}_n(t_0 + T; t_0, \mathbf{x}_0) \perp T_{\mathbf{x}_0} \mathcal{M}(t_0)$,
3. $\nabla \lambda_n(t_0 + T; t_0, \mathbf{x}_0) \cdot \boldsymbol{\xi}_n(t_0 + T; t_0, \mathbf{x}_0) = 0$,
4. $\mathbf{L}(t_0 + T; t_0, \mathbf{x}_0)$ positive definite for all $\mathbf{x}_0 \in \mathcal{M}(t_0)$.

$$\mathbf{L} = \begin{bmatrix} \nabla^2 \Delta^{-1}[\boldsymbol{\xi}_n, \boldsymbol{\xi}_n, \boldsymbol{\xi}_n, \boldsymbol{\xi}_n] & 2 \frac{\lambda_n - \lambda_1}{\lambda_1 \lambda_n} (\boldsymbol{\xi}_1 \cdot \nabla \boldsymbol{\xi}_n \boldsymbol{\xi}_n) & \cdots & 2 \frac{\lambda_n - \lambda_{n-1}}{\lambda_{n-1} \lambda_n} (\boldsymbol{\xi}_{n-1} \cdot \nabla \boldsymbol{\xi}_n \boldsymbol{\xi}_n) \\ 2 \frac{\lambda_n - \lambda_1}{\lambda_1 \lambda_n} (\boldsymbol{\xi}_1 \cdot \nabla \boldsymbol{\xi}_n \boldsymbol{\xi}_n) & \frac{2\lambda_n - \lambda_1}{\lambda_1 \lambda_n} & \cdots & 0 \\ \vdots & \vdots & \ddots & \vdots \\ 2 \frac{\lambda_n - \lambda_{n-1}}{\lambda_{n-1} \lambda_n} (\boldsymbol{\xi}_{n-1} \cdot \nabla \boldsymbol{\xi}_n \boldsymbol{\xi}_n) & 0 & \cdots & \frac{2\lambda_n - \lambda_{n-1}}{\lambda_{n-1} \lambda_n} \end{bmatrix}$$

with

$$\nabla^2 \Delta^{-1}[\boldsymbol{\xi}_n, \boldsymbol{\xi}_n, \boldsymbol{\xi}_n, \boldsymbol{\xi}_n] = -\frac{1}{\lambda_n^2} (\boldsymbol{\xi}_n \cdot \nabla^2 \lambda_n \boldsymbol{\xi}_n) + 2 \sum_{q=1}^{n-1} \frac{\lambda_n - \lambda_q}{\lambda_n \lambda_q} (\boldsymbol{\xi}_q \cdot \nabla \boldsymbol{\xi}_n \boldsymbol{\xi}_n)^2.$$

This is a general formulation valid for a n -dimensional problem. The conditions can be reformulated for a 2D problem taking into account numerical sensitivity and implementation robustness [7]:

- A. $\lambda_1(t_0 + T; t_0, \mathbf{x}_0) \neq \lambda_2(t_0 + T; t_0, \mathbf{x}_0) > 1$,
- B. $\boldsymbol{\xi}_1(t_0 + T; t_0, \mathbf{x}_0) \parallel \mathcal{M}(t_0)$,
- C. $\bar{\lambda}_2(\gamma)$, the average of λ_2 over a curve γ , is maximal on $\mathcal{M}(t_0)$ among all nearby curves γ satisfying $\gamma \parallel \boldsymbol{\xi}_1(t_0 + T; t_0, \mathbf{x}_0)$,
- D. $\boldsymbol{\xi}_2(t_0 + T; t_0, \mathbf{x}_0) \cdot \nabla^2 \lambda_2(t_0 + T; t_0, \mathbf{x}_0) \boldsymbol{\xi}_2(t_0 + T; t_0, \mathbf{x}_0) < 0$.

According to condition B, repelling LCSs are material curves tangent to $\boldsymbol{\xi}_1$, the eigenvector field associated with the smaller eigenvalue of CG strain tensor. Lines tangent to $\boldsymbol{\xi}_1$ are called strainlines. Numerical algorithms that implement Haller variational theory are based on the computation of strainlines which constitute a LCSs candidates set. Then a filtering process is applied to extract LCSs. Keep note that this formulation is valid for a repelling LCS. In order to compute attracting LCSs a similar procedure can be adopted. As counterparts of strainlines, stretchlines are the curves of the phase space that present compressing forces and are linked to attracting LCSs [7].

4.5. Lagrangian descriptors

LDs were recently introduced as a powerful tool capable of revealing LCSs and underlining the geometrical template of phase space structures for a generic dynamical system [27]. The simple idea behind LDs is to seed a given phase space region with ICs and integrate a bounded, positive property of the trajectory for a finite time interval. LDs have the capability to provide a qualitative description of the system's dynamics and reveal the skeleton governing phase space transport.

The first mathematical definition of LD relied on the computation of the arclength of particle trajectories as they evolve forward and backward in time [26], until after the method has been extended to others positive quantities. At its origins, LD approach was implemented as a tool to provide a definition of distinguished hyperbolic trajectories. They are the generalization of the concept of saddle fixed point of autonomous systems into time-dependent ones [26]. Distinguished hyperbolic trajectories were highlighted by minima of the descriptor function. Applicability of LD approach has been extended to the detection of invariant manifolds of hyperbolic trajectories [27]. Invariant manifolds were highlighted by "singular features", or "abrupt changes", of the LD field. The methodology has found a myriad of applications in different scientific areas. LDs were implemented to analyze oil spill transport in a region of the Gulf of Mexico [29]. In a similar way, authors of [10] used these tools for the real-time management of oil spills in Spain, close to Canary Islands. In addition, descriptors has been exploited to study transport mechanisms in the stratospheric polar vortex [9]. These instruments found their application also in chemistry, to study the phase space objects that control transport in exothermic reactions [12].

Consider a general time-dependent vector field

$$\frac{d\mathbf{x}}{dt} = \mathbf{v}(\mathbf{x}, t), \quad \mathbf{x} \in \mathbb{R}^n, \quad t \in \mathbb{R}. \quad (4.13)$$

Assuming that the velocity field is C^r ($r \geq 1$) in \mathbf{x} and continuous in t , unique solutions that also allow for linearization exist. Original LD formulation was linked to the trajectory length of the particle [26]. Specifically, let's define M as the Euclidean arc length of the curve in the phase space defined by the propagation of an initial state \mathbf{x}_0 through Eq. (4.13). Setting an integration time interval $[t_0 - \tau, t_0 + \tau]$ [27],

$$M(\mathbf{x}_0, t_0, \tau) = \int_{t_0 - \tau}^{t_0 + \tau} \sqrt{\sum_{i=1}^n \left(\frac{dx_i(t)}{dt} \right)^2} dt = \int_{t_0 - \tau}^{t_0 + \tau} \|\mathbf{v}(\mathbf{x}, t)\| dt, \quad (4.14)$$

$$M(\mathbf{x}_0, t_0, \tau) = M^{(b)}(\mathbf{x}_0, t_0, \tau) + M^{(f)}(\mathbf{x}_0, t_0, \tau) = \int_{t_0 - \tau}^{t_0} \|\mathbf{v}(\mathbf{x}, t)\| dt + \int_{t_0}^{t_0 + \tau} \|\mathbf{v}(\mathbf{x}, t)\| dt. \quad (4.15)$$

Notice that the definition of function M can be broken in a natural way into forward ($M^{(f)}$) and backward ($M^{(b)}$) contributions. Forward integration would highlight the stable manifolds of an autonomous dynamical system, while backward evolution would recover the unstable ones [8]. Moreover, their combination detects all the invariant manifolds simultaneously. Trajectories with close initial conditions that remain close as they evolve on

the time interval are expected to have similar value of M . Subsequently, the boundaries between regions comprising trajectories with qualitatively different behaviour should denote an abrupt change of the derivative of M transverse to these boundaries [22]. Sharp changes in the scalar field of LD are labeled as "singular structures". It is important to remark the crucial role of integration time τ . The more τ value increases, the more structures will appear and the more information will be contained in the field. However, for small τ values, the pattern revealed by the descriptor field may not match the actual phase space structures of the system [27].

There are other positive intrinsic physical or geometric properties of trajectories that can be integrated bringing to successful results. The generalized LD formulation can be written as [27]

$$M(\mathbf{x}_0, t_0, \tau) = \int_{t_0-\tau}^{t_0+\tau} |\mathcal{F}(\mathbf{x}(t))|^\gamma dt. \quad (4.16)$$

Integrand $|\mathcal{F}(\mathbf{x}(t))|^\gamma$ denotes a bounded, positive property of the state vector, with γ the exponent that defines its norm. A key property of all the descriptors is that they are quantities that accumulate along a trajectory, i.e. they are integrals of a positive quantity. Being a heuristic approach, like FTLE field, there is no certainty that this tool identifies LCSs correctly, since there are no precise mathematical conditions embedded in LD theory like in the variational theory. However, efforts to provide a theoretical framework for LDs have been done. In [22], the authors formulated rigorous proofs to show the ability of the descriptors to reveal stable and unstable manifolds of hyperbolic points in simple two-dimensional systems. LD is an intuitive, easy to implement and computationally efficient visual tool, which can give lot of information on the dynamics of the problem. A straightforward strategy to numerically compute the descriptor is to augment the state vector \mathbf{x} in Eq. (4.13) such that $\dot{x}^{(n+1)} = |\mathcal{F}(\mathbf{x}(t))|^\gamma$ and propagate \mathbf{x}_0 in the $[t_0 - \tau, t_0 + \tau]$ interval. It follows that $x^{(n+1)}(t_0 + \tau) = M(\mathbf{x}_0, t_0, \tau)$. Algorithm 2 describes the procedure to compute the LD field for a given phase space domain $G \subset \mathbb{R}^n$ and visualize it in the two-dimensional subspace of interest.

Algorithm 2 LD visualization algorithm

- 1: G is the grid of initial conditions in the phase space
 - 2: $[t_0 - \tau, t_0 + \tau]$ is the integration time interval
 - 3: **for** each $\mathbf{x}_0 \in G$ **do**
 - 4: Propagate augmented dynamics
 - 5: Extract $M(\mathbf{x}_0, t_0, \tau)$
 - 6: **end for**
 - 7: Plot $M(\mathbf{x}_0, t_0, \tau)$, $\forall \mathbf{x}_0 \in G$, in the two-dimensional subspace of interest
-

4.6. The Duffing oscillator example

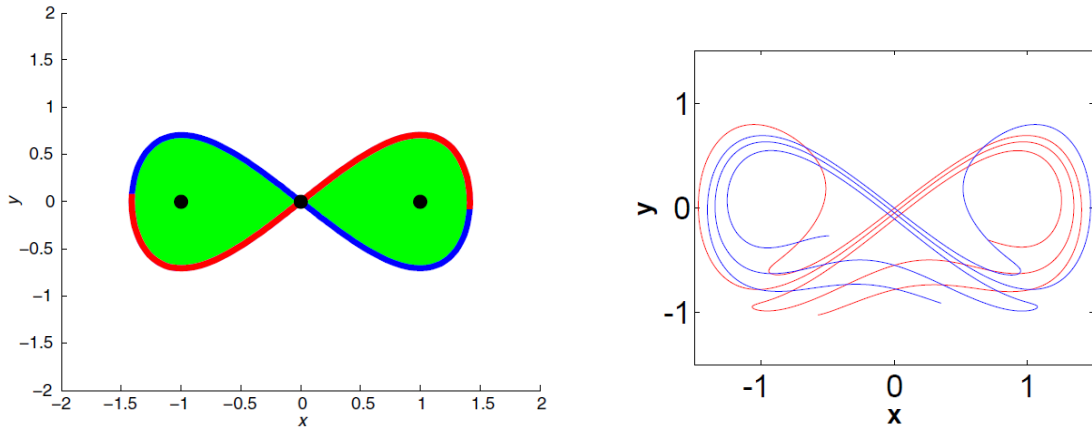
The ability of FTLE and LD approaches in highlighting manifolds is examined on a toy problem. The selected problem is the Duffing oscillator [27], whose equations of motion read

$$\begin{cases} \dot{x} = y, \\ \dot{y} = x - x^3 + \epsilon f(t). \end{cases} \quad (4.17)$$

Two cases are considered:

Autonomous case ($\epsilon = 0$). The system has three equilibrium points, one unstable at the origin and two marginally stable at $(\pm 1, 0)$. The origin is an hyperbolic saddle point connected by its stable and unstable manifolds. Manifolds form two homoclinic orbits, as shown in Fig. 4.8a.

Periodically forced case ($\epsilon = 0.1$ and $f(t) = \sin(t)$). The system has a hyperbolic periodic trajectory near the origin referred as distinguished hyperbolic trajectory with its stable and unstable manifolds segments (Fig. 4.8b) [26].



(a) Equilibria (black), global stable (blue) and unstable (red) manifold of the origin in the autonomous case, taken from [30].

(b) Stable (blue) and unstable (red) manifold in the periodically forced case, taken from [27].

Figure 4.8: Stable and unstable manifolds of Duffing oscillator.

The chosen phase space domain is $G = [-1.5, 1.5] \times [-1.5, 1.5]$ with $[300 \times 300]$ grid points. The same grid is used for both FTLE and LD fields computation. Final integration time is set to $\tau = 10$, while $t_0 = 0$. Exploitation of the FTLE technique allows to capture the presence of stable and unstable manifolds in both cases. The FTLE field computed in forward time over a grid of initial conditions presents ridges in correspondence of stable manifolds, which can be appreciated in Fig. 4.9. In the same way a backward integration would highlight unstable manifolds.

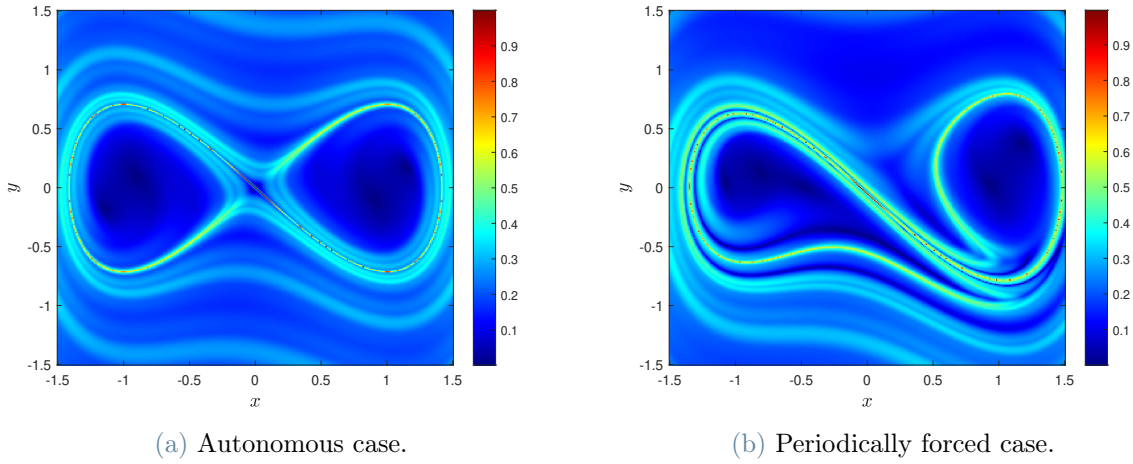


Figure 4.9: FTLE fields of Duffing oscillator.

The LD field is able to catch stable and unstable manifolds in the phase space, as long as choosing a sufficiently long integration time. A contour plot of the field is shown in Fig. 4.10a. Manifolds are located at points where M scalar values change abruptly (Fig. 4.10b).

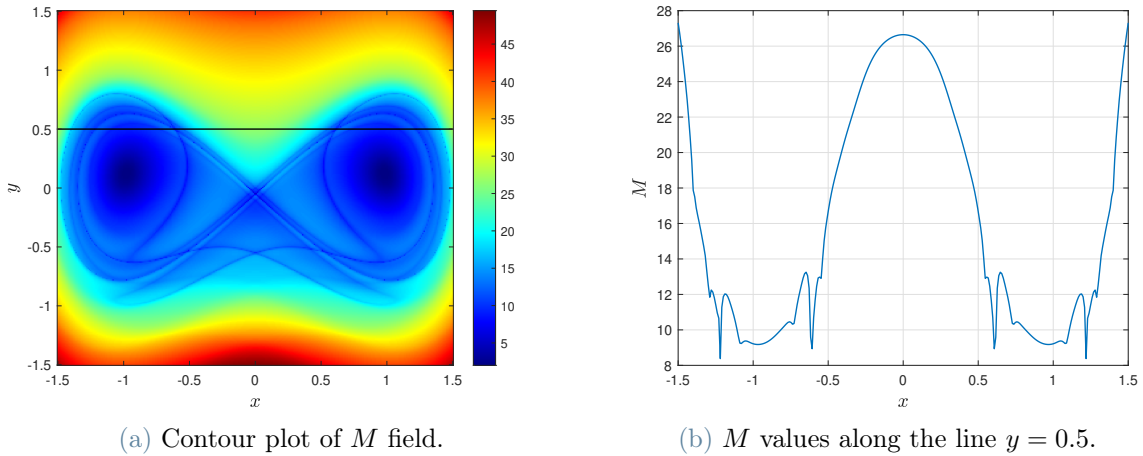


Figure 4.10: LD field of forced Duffing oscillator.

Compared to FTLE field, LDs provide in general superior performance, in the sense that they more accurately reveal geometrical structures and require less computational effort to converge to them [27]. Calculation of FTLE requires the integration of variational equations of motions, which is more computational intensive than computing the LD. Another advantage is that the LD technique is able to reveal at the same time stable and unstable manifolds of the system.

4.7. Applications to ballistic capture

Different studies investigated LCSs applied to the restricted three-body problem in the frame of ballistic capture. In the CR3BP context, FTLE fields are able to reveal the intersections of invariant manifolds of periodic orbits with Poincaré cuts [11], whose classical computation procedure has been presented in Section 2.1.1. Fig. 4.11 compares the outputs of the two procedures.

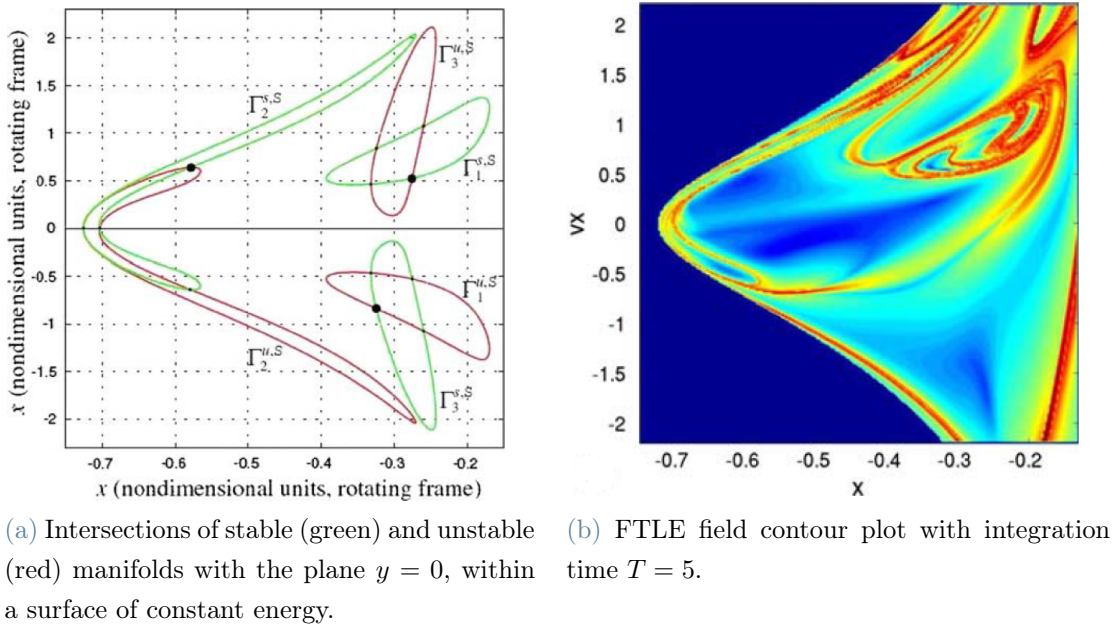


Figure 4.11: Invariant manifolds intersections in the CR3BP [11].

Fig. 4.11a shows the intersections of invariant manifold tubes of a Lyapunov orbit around L_1 for a fixed energy level. As expected, FTLE ridges can be observed in correspondence of intersections of the stable manifold ($\Gamma_i^{s,S}$). Increasing the integration time, higher order intersections are revealed. FTLE approach becomes helpful when the ER3BP model is taken into account. In [11], authors demonstrated the existence of periodically pulsating LCSs in the phase space of the ER3BP exploiting FTLE method. These pulsating structures proved to be the time-dependent analogues of invariant manifolds of periodic orbits in the circular problem.

FTLE fields can also be used as visual detection tool to locate the WSB of stable sets [31]. WSBs play the role of dynamics separatrices, distinguishing phase space regions of ICs generating orbits with different global behaviour. Fig. 4.12 displays an FTLE field computed in a phase space region around Mars and within the planar ER3BP assumption.

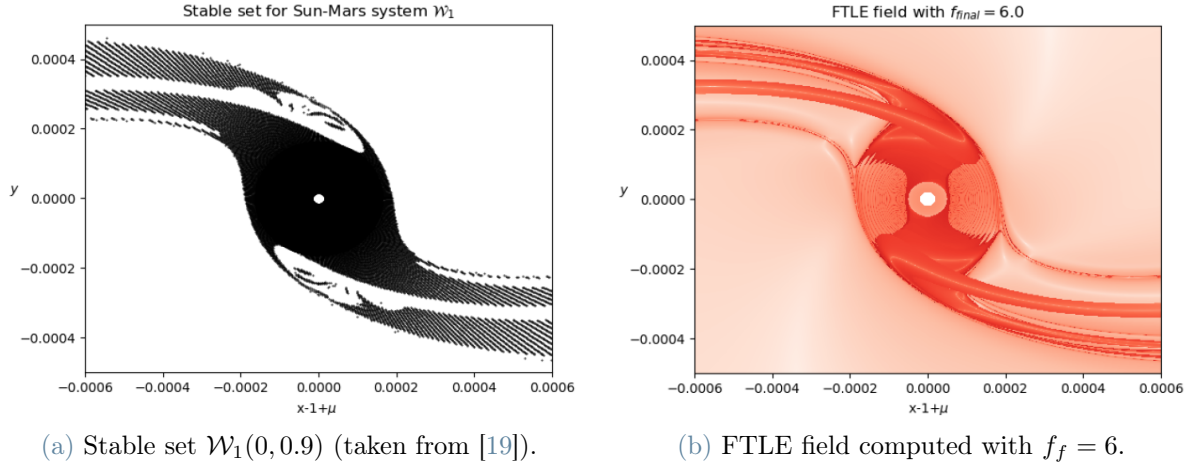


Figure 4.12: FTLE field for the Sun–Mars ER3BP and $\mathcal{W}_1(0, 0.9)$ comparison [31].

The field clearly resembles the stable set. The latter has been computed outside this research, obtained according to the methodology described in [19]. FTLE field proves to be an efficient tool to get an idea of the shape of the WSB. LCSs extraction from variational theory has also been applied to the computation and understanding of ballistic capture trajectories in the area of stable sets manipulation [28, 31, 33]. As shown in Fig. 4.13, repelling LCSs obtained with variational theory match with the boundaries at the right and the left wings of the sets. However, correspondence between the strainlines and the

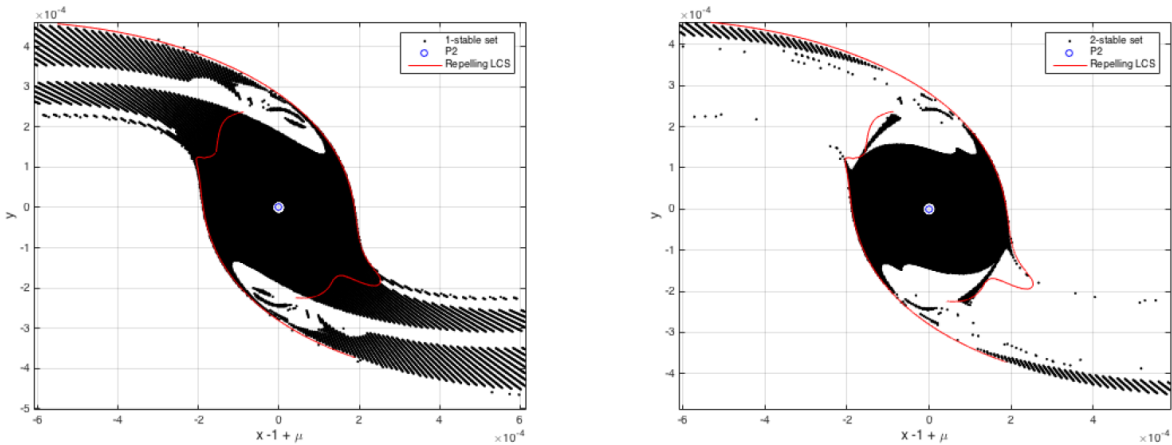


Figure 4.13: Repelling LCS overlapped to stable sets $\mathcal{W}_1(0, 0.9)$ and $\mathcal{W}_2(0, 0.9)$ (courtesy of N. Hyeraci, and F. Topputo [19]) of Sun–Mars system [33].

WSB is not perfect. This could be caused by the high sensitivity of LCSs to different particle dynamics and by the fact that structures are computed using a fixed integration time [31]. Indeed, the final integration time of each particle in the stable sets computed

in [19] is not constant. In conclusion, LCSs extracted with variational theory give an idea of the WSB shape but matching is not completely satisfactory.

4.8. LCSs extraction strategies trade-off

This section shows a comparison of the various LCSs extraction techniques discussed so far. The aim is to find the best approach suited to the case study addressed in this thesis. FTLE, variational theory, and LD approaches are compared according to some selection criteria. Chosen criteria are: reliability in LCSs detection, implementation simplicity, and computational speed.

Variational theory is the most reliable approach since it assures that the extracted LCSs satisfy precise mathematical definitions. However, the extraction procedure is complicated and requires a big computational effort. It requires not only the integration of the variational equations, but also the computation and filtering of strainlines and stretchlines [7]. FTLE approach presents some inconsistencies in the LCSs detection. It is simple to implement but requires the integration of variational equations. FTLE is connected to the LCS definition by the computation of the maximum eigenvalue of CG strain tensor. The LD method lacks of explicit mathematical connection with LCSs, but different studies proved the ability of LDs to detect invariant manifolds in simple dynamical systems [22, 27]. LDs implementation is simple and intuitive and does not require the propagation of the variational set of equations.

These considerations are translated into numerical values associated with each criterion for each LCSs extraction technique. The value 1 represents a bad performance, while 3 is associated with a good one. Comparison is reported in Tab. 4.1. The sum of each score associated to each criterion represents the global performance of the technique. The result justifies the implementation of the LD strategy compared to the other ones in the case study under examination.

Table 4.1: Performance comparison between LCSs extraction techniques.

	Variational theory	FTLE	LD
Reliability in LCS detection	3	2	2
Implementation simplicity	1	2	3
Computational speed	1	2	3
Global performance	5	6	8

5 | Ballistic capture at Mars via Lagrangian descriptors

The LD approach is now applied in the Sun–Mars ER3BP in order to verify to what extent this technique provides a characterization of the dynamics in Mars proximity with regard to ballistic capture. Motivations rely on the fact that LDs have the potential to be an efficient tool to infer the dynamics of phase space regions about the target. It could help in the design of ballistic orbits offering new perspectives. The final research objective is to exhibit the correlation between the geometrical template extracted from LD fields in the phase space region around Mars and the WSBs of classification sets.

5.1. Definition of classification sets

The general procedure to categorize each IC in the domain of interest derives from [24], which is the one described in Chapter 3. In this thesis, an alternative definition of stable sets is proposed. Basically, the number of revolutions of the particle around the target planet is no more considered. As a result, stability numbers n disappear and only three subsets are present. While propagating ICs in the non-dimensional synodic reference frame (see Section 2.2) in the integration interval $[f_0, f_f]$, a classification algorithm computes the non-dimensional distance and Kepler energy of the particle with respect to Mars. Classification is based on the fulfillment of some conditions that take distance and energy as input and verify if the particle escapes from the planet or impacts on its surface. With this procedure every initial state is collocated in one of three complementary subsets (\mathcal{X} , \mathcal{K} , and \mathcal{W}) depending on its dynamics. Classification sets are defined in the following list:

Escape set $\mathcal{X}(f_f)$ contains ICs whose orbits escape for $f \leq f_f$. The particle escapes if it possesses positive Kepler energy with respect to Mars and, at the same time, is located outside the planet sphere of influence (SOI). In the elliptic problem the

Kepler energy reads [19]

$$H(f) = \frac{1}{2}v^2(f) - \frac{\mu}{r(1 + e_p \cos f)}, \quad (5.1)$$

where v can be re-arranged using polar coordinates as

$$v^2(f) = \left(\frac{r e_p \sin f}{1 + e_p \cos f} + r' \right)^2 + r^2(1 + \theta')^2. \quad (5.2)$$

Notice that H depends on the current value of f . So, even if the state is constant, its Kepler energy relative to the target varies according to the mutual motion of primaries. In conclusion, the two conditions that must be satisfied at the same time are

$$\begin{cases} H(f) > 0, \\ r(f) > R_s, \end{cases} \quad (5.3)$$

where R_s is the non-dimensional SOI radius of the target.

Crash set $\mathcal{K}(f_f)$ contains ICs whose orbits crash for $f \leq f_f$. The particle impacts if its distance from Mars surface is negative, or equivalently

$$r(f) < R_{eq}. \quad (5.4)$$

R_{eq} represents the non-dimensional mean equatorial radius of the planet.

Weakly stable set $\mathcal{W}(f_f)$ contains ICs whose orbits do not escape or crash for $f \leq f_f$.

Keep note that the ER3BP equations of motion in Eq. (2.9) are integrated in Cartesian coordinates, but stability conditions are based on polar ones. Therefore, at each integration step, a coordinates transformation $S2P$ from Cartesian, or synodic, to polar coordinates must be performed

$$S2P(x, y, x', y') = \begin{cases} r = \sqrt{(x - 1 + \mu)^2 + y^2} \\ \theta = \arctan\left(\frac{y}{x - 1 + \mu}\right) \\ r' = x' \cos \theta + y' \sin \theta \\ \theta' = \frac{-x' \sin \theta + y' \cos \theta}{r} \end{cases} \quad (5.5)$$

r and θ are the polar coordinates of the particle with respect to Mars (P_2 in Fig. 5.1).

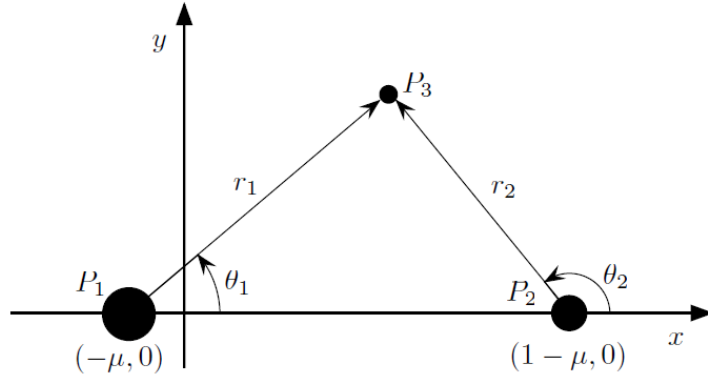


Figure 5.1: Synodic reference frame and polar coordinates [19].

In analogy with the capture set definition given in Chapter 3, an alternative formulation of \mathcal{C} is derived. A capture set is extracted from the intersection between an escape set \mathcal{X} obtained propagating dynamics backwards and a weakly stable set \mathcal{W} obtained integrating forwards.

$$\mathcal{C}(f_B, f_F) = \mathcal{X}(f_B) \cap \mathcal{W}(f_F). \quad (5.6)$$

An IC belonging to $\mathcal{C}(f_B, f_F)$ generates an orbit that escapes from the target planet before reaching f_B if integrated backward, while remains bounded into the region of influence of Mars without crashing at least until f_F if integrated forward.

5.2. Lagrangian descriptors computation

LD definition given in Eq. (4.16) is now adapted to the ER3BP in the study case. The mathematical formulation of the descriptor implemented in this research reads

$$M(\mathbf{x}_0, f_0, f_F, f_B) = \int_{f_0}^{f_0+f_F} |\mathcal{F}(\mathbf{x}(f))|^\gamma df + \int_{f_0-f_B}^{f_0} |\mathcal{F}(\mathbf{x}(f))|^\gamma df. \quad (5.7)$$

ER3BP equations of motion can be rearranged as a four-dimensional ordinary differential equations system

$$\begin{cases} x' = v_x, \\ y' = v_y, \\ x'' = 2v_y + \omega_x, \\ y'' = -2v_x + \omega_y. \end{cases} \quad (5.8)$$

The initial state vector reads $\mathbf{x}_0 = [x_0, y_0, x'_0, y'_0]$. The particle is initially set at the perapsis of an osculating prograde ellipse around Mars, with a given eccentricity e . Values of

$e \in [0.9, 1)$ are optimal to retrieve ballistic capture trajectories as suggested by numerical experiments in [19]. From this assumption the full initial state \mathbf{x}_0 of each IC in the domain of interest can be retrieved.

The integrand $|\mathcal{F}(\mathbf{x}(f))|^\gamma$ denotes a bounded, positive property of the state vector, with γ the exponent that defines its norm. Different integrands have been implemented and tested in this research, they are listed in Tab. 5.1. In the integrands definition, $\mathbf{v} = [x', y']$ and $\mathbf{a} = [x'', y'']$ represent first and second derivatives of the position vector with respect to f ; κ is the curvature of the trajectory that combines \mathbf{v} and \mathbf{a} . The value ranges from zero (curvature of a straight line) to infinity (curvature of a point) [27]. Keep note that \mathbf{v} and \mathbf{a} do not express velocity and acceleration of the particle in strict sense since the differentiation is done with respect to f and not t .

Table 5.1: Implemented Lagrangian descriptors.

Descriptor	Integrand	Norm
M_1	$\mathcal{F}_1 = \mathbf{v}$	$\gamma = 1$
M_2	$\mathcal{F}_2 = \mathbf{a}$	$\gamma = 1$
M_3	$\mathcal{F}_3 = \mathbf{v}$	$\gamma = 1/2$
M_4	$\mathcal{F}_4 = \mathbf{a}$	$\gamma = 1/2$
M_5	$\mathcal{F}_5 = \frac{1}{\kappa+1}$, where $\kappa = \frac{\sqrt{(\mathbf{v}\cdot\mathbf{v})(\mathbf{a}\cdot\mathbf{a}) - (\mathbf{v}\cdot\mathbf{a})^2}}{(\mathbf{v}\cdot\mathbf{v})^{3/2}}$	$\gamma = 1$

The LD field is generated evaluating the integral per each \mathbf{x}_0 of a computational grid in a specific domain, so every grid point in the phase space is linked to a positive scalar value. The computational grid of ICs is denoted as G . Thus, $M(G, f_0, f_F, f_B)$ represents the LD field computed for all the grid points. A contour plot in the position subspace (x, y) is then performed to underline some boundaries, denoted by "abrupt changes" of the field. An abrupt change means that the derivative of M field transverse to these boundaries is discontinuous on them. These singular features coincide with phase space structures that separate orbits with different dynamics.

Notice that the LD definition $M(\mathbf{x}_0, f_0, f_F, f_B)$ in Eq. (5.7) has two contributions. The forward time contribution $M(\mathbf{x}_0, f_0, f_F, 0)$ isolates dynamics separatrices generated in forward time which are linked to repelling LCSs of the dynamical system. Similarly, $M(\mathbf{x}_0, f_0, 0, f_B)$ highlights the attracting LCSs of the system, isolating separatrices in backward time. LDs fields are computed for different values of f_F and f_B . Similar results have been obtained for all descriptors with the same final integration limits and will be presented in Chapter 6. In the problem at hand, M_3 field manifested a clearer

visual separation of phase space regions than the other descriptors. A visual proof of this statement is reported in Chapter 6. For this reason M_3 is taken as reference LD in the dynamics separatrices extraction phase.

5.2.1. Consideration on the integration limits

An investigation has been performed in order to find the proper final integration time per each grid point in the LD computation to achieve a good match between highlighted regions in the LD field and stable sets computed by the authors of [19]. Fig. 5.2 displays $\mathcal{W}_1(f_0, e)$ and $\mathcal{W}_3(f_0, e)$ stable sets for the planar Sun-Mars ER3BP. They have been obtained setting an initial anomaly of $f_0 = 0$ and eccentricity of the initial osculating orbit $e = 0.9$ (see [19] for further details).

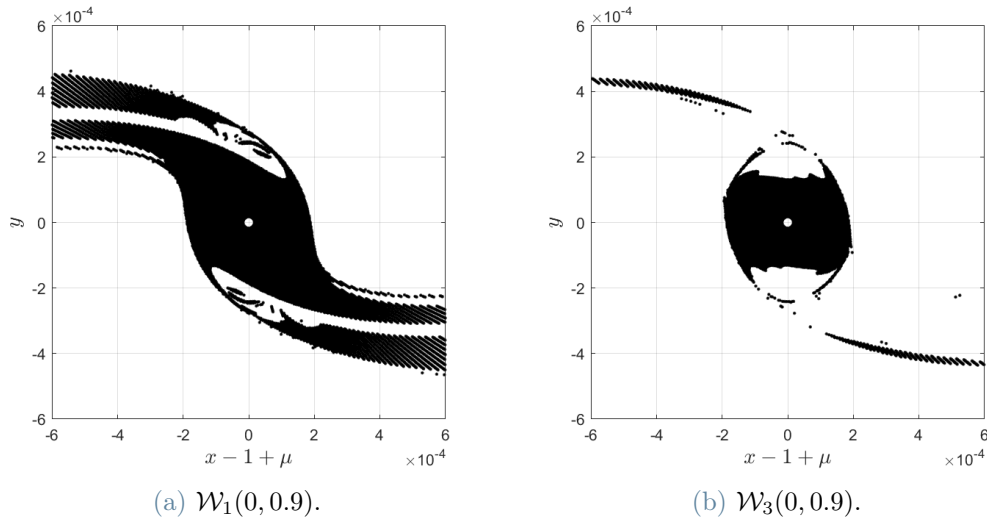


Figure 5.2: Stable sets of Sun–Mars ER3BP (courtesy of N. Hyeraci, and F. Topputo [19]).

The provided strategy consists in adopting a variable final integration anomaly which depends on the distance of the IC from Mars. In the stable sets manipulation technique implemented in [19], the integration limit is not constant for all the domain. An IC is integrated until it reaches a given number of revolutions around the target primary. Specifically, the stable set \mathcal{W}_n contains ICs whose trajectory perform n revolutions around the target in the synodic frame with a negative Kepler energy at each revolution. As rule of thumb, stable ICs which are more distant from Mars need more time to complete a revolution compared with closer conditions. This concept is now applied to LD field computation with the purpose of revealing WSBs of stable sets \mathcal{W}_n .

As first trial, a final anomaly f_F proportional to the period of a Keplerian orbit around the target is investigated. As an assumption, a particle temporarily captured by the planet is expected to fly on a trajectory resembling a Keplerian orbit. The dimensional period of the initial osculating orbit around Mars with eccentricity e reads

$$T = 2\pi \sqrt{\frac{a^3}{\mu_M}} = 2\pi \frac{r_p^{3/2}}{\sqrt{\mu_M(1-e)^3}} = 2\pi \frac{R_{12}(f_0)r_0^{3/2}}{\sqrt{\mu_M(1-e)^3}}, \quad (5.9)$$

where μ_M is Mars gravitational constant, while $R_{12}(f_0)$ the primaries distance at f_0 , needed to obtain the initial non-dimensional distance r_0 of the particle from Mars (the non-dimensionalization strategy was introduced in Chapter 2). The non-dimensional period can be written as

$$\tilde{T} = 2\pi \frac{R_{12}(f_0)r_0^{3/2}}{\sqrt{\mu_M(1-e)^3}} \sqrt{\frac{\mu_S}{a_p^3}} = K \cdot r_0^{3/2}, \quad (5.10)$$

where μ_S is Sun gravitational constant. The non-dimensional period is assumed to be the final anomaly f_F . This is true in the case of the circular problem, but the correction would not considerably affect proportionality of f_F with respect r_0 . Correction can be performed integrating Eq. (2.8) to obtain the anomaly corresponding to \tilde{T} . As result, this strategy implies a f_F that increases with the non-dimensional distance from the target. Different simulations have been performed setting multiples of K in the integration limit. Overall, the approach does not appear successful in providing phase space regions resembling the stable sets in Fig. 5.2. Conditions far from Mars show their dynamical behaviour before than nearer points. This causes an inhomogeneity of the structures inside the domain of interest. The reason is that behaviour of stable points further from Mars is far to be close to a Keplerian one.

A trial and error strategy led to a change of the r_0 exponent, and a dependence of $f_F = A\sqrt{r_0}$ proved to be a good solution for the purpose of this investigation. Evolution of phase space structures in the descriptor fields for increasing values of A is uniform all over the domain. The mentioned two functions relating f_F and r_0 are shown in Fig. 5.3. Contour plots of M_1 field computed with both functions are presented in Fig. 5.4. Boundaries revealed in Fig. 5.4a qualitatively correspond to \mathcal{W}_1 borders. A good match with \mathcal{W}_3 is obtained from the regions highlighted by M_4 field computed with $f_F = 200\sqrt{r_0}$, as displayed in Fig. 5.5.

Nevertheless, results obtained with constant f_F are acceptable and do not differ so much from those obtained with a variable final anomaly. In the following steps of the methodology, in order to reveal stable sets boundaries, the same integration limit will be adopted per each initial state in the domain.

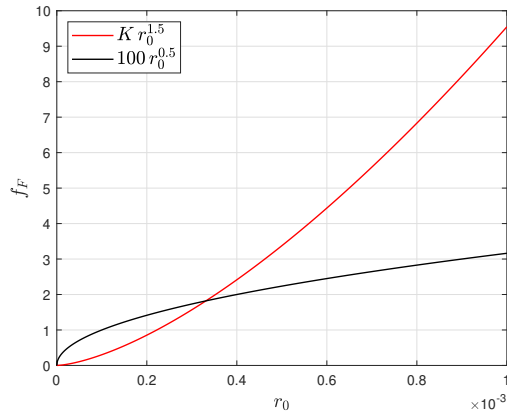


Figure 5.3: Final anomaly functions.

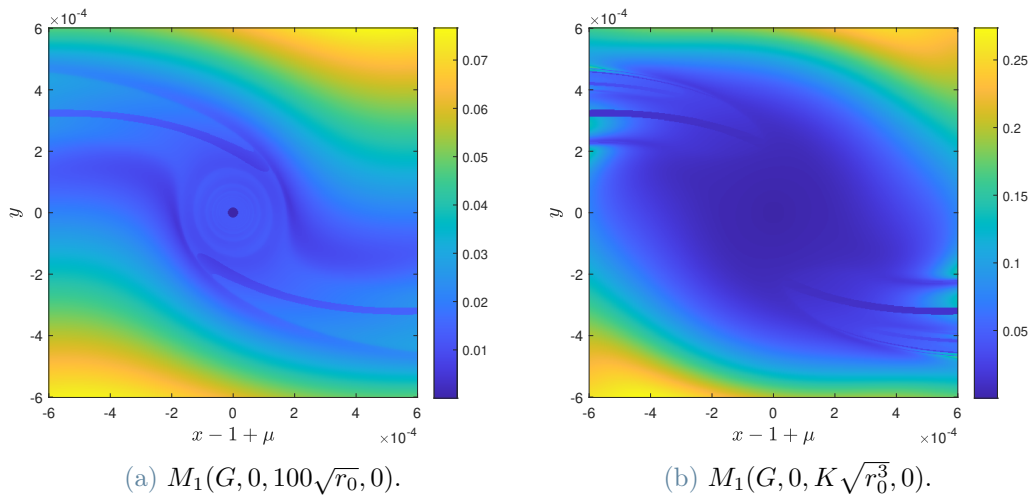


Figure 5.4: M_1 contour plots for different f_f functions.

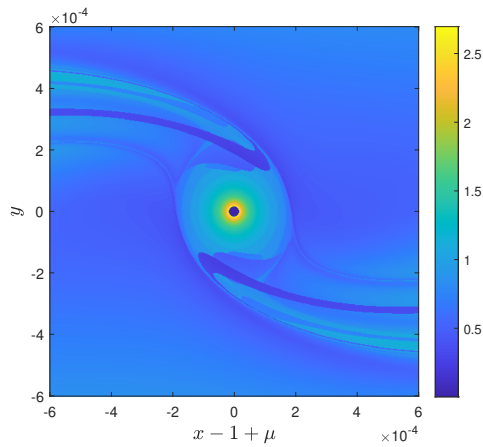


Figure 5.5: $M_4(G, 0, 200\sqrt{r_0}, 0)$.

5.3. Separatrices extraction

Singular structures revealed by LD fields are extracted with an edge detection algorithm. Edge detection is an image processing technique usually exploited for finding boundaries of objects within images [1]. An edge is defined as the locus of points in which there is a rapid change in intensity of the image. Edge detection methods highlight discontinuities exploiting one of the two criteria reported below:

- methods finding edges at those points where the first derivative of the intensity is larger than a threshold value σ ;
- methods finding edges at those points where the second derivative of the intensity has a zero crossing. Depending on the selected threshold, a large jump across zero is an edge, while a small jump is not.

There are several edge detection algorithms available which differ according to the criterion with whom they detect discontinuities. Some of them are Sobel, Prewitt, Roberts, Canny and zero-cross methods [1].

Different methods have been tested for this study case. Roberts proved to be the most effective one by revealing the edges more clearly than the others. A comparison between the methods is reported in Chapter 6. The algorithm takes as input the two-dimensional contour plot of the descriptor field in the (x, y) subspace of the domain. Then it finds edges at those points where the gradient magnitude of the image is higher than a threshold value using the Robert approximation to the derivative. Specifically, gradient of the image is approximated by computing the sum of the squares of the differences between diagonal neighbors pixels [32].

As anticipated, an additional input of edge detection algorithms is the sensitivity threshold σ . For gradient magnitudes larger than the threshold, the algorithm ignores those edges. The edge detection gives as output a binary image of the same size of LD scalar field, with 1s where the algorithm finds edges and 0s elsewhere. For each computed descriptor field the value of threshold is tuned. It is adjusted in order to show the highest number of structures revealed by abrupt changes in the field. However, too low values of the threshold itself could generate false positives in the output binary image when compared to the LD contour plot.

5.4. Validation of extracted separatrices

Ideally, extracted dynamics separatrices from LD field are expected to match exactly with the boundaries between the classification sets \mathcal{X} , \mathcal{K} , \mathcal{W} for a given integration interval. The reason is that the LD should be able to catch the dynamical divergence in trajectories between different classification sets. Borders of classification sets are also referred as the WSBs, in accordance with the nomenclature used in literature. Note that the definition of WSB used in this research refers to the borders of sets characterized by the same dynamic behaviour. It does not need necessarily to be linked to a stable set. The flowchart in Fig. 5.6 summarizes the workflow designed to validate extracted patterns.

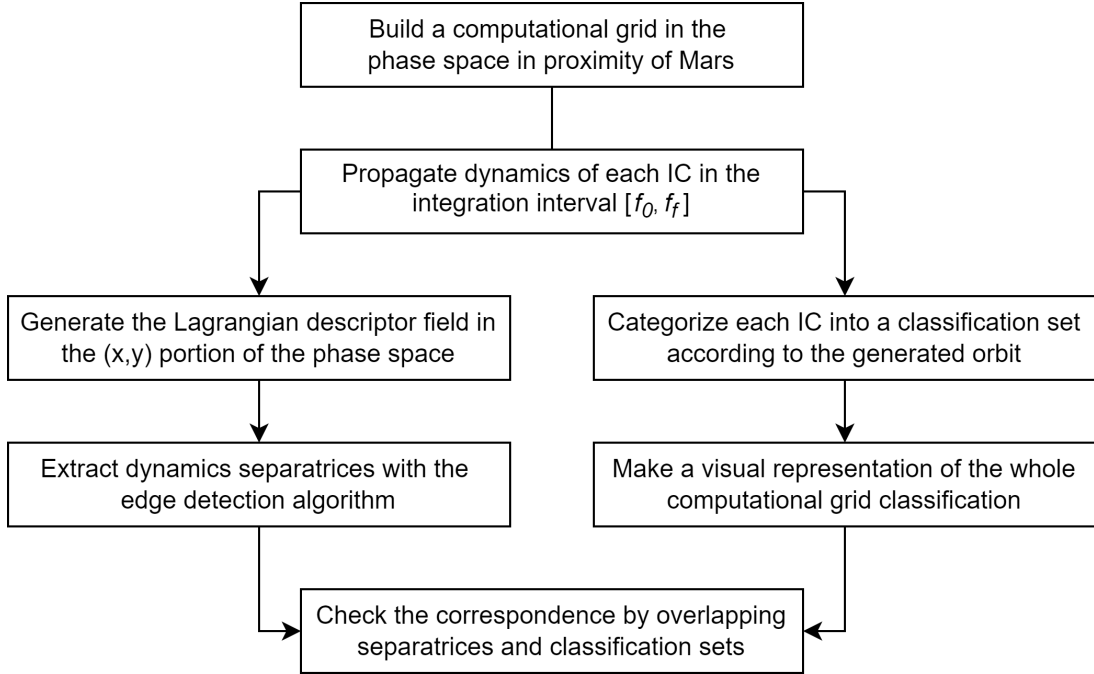


Figure 5.6: Validation workflow.

The first step is to build a computational grid of ICs around Mars. Two basic elements characterize it: boundaries of the domain of interest and the number of grid points. The grid is built in the synodic frame centered at the target at f_0 . In the presented study this reference frame is also referred as the inertial frame. Boundaries of the domain of interest are selected according to the knowledge of stable sets of the Sun–Mars system computed by the authors in [19]. The selected portion of the (x, y) domain allow to appreciate the differences between stable sets with distinct stability numbers. Moreover, the same boundaries have been chosen by the authors of [31, 33] to study LCSs applied to ballistic capture at Mars (Figs. 4.12 and 4.13). The number of grid points is selected

as a compromise between computational effort and the visual quality of LD fields and classification sets.

Grid points positions in the inertial frame are expressed as $[\tilde{x}_0, \tilde{y}_0]$ coordinates. Since the ER3BP dynamics is propagated in the synodic reference frame, a coordinates transformation is needed. In addition, the full initial state of four components is retrieved in polar coordinates $[r_0, \theta_0, r'_0, \theta'_0]$ with respect to the target [19]. The procedure is schematized as a block scheme in Fig. 5.7, where *I2P* (inertial to polar) and *P2S* (polar to synodic) are two functions that perform the coordinates transformation.

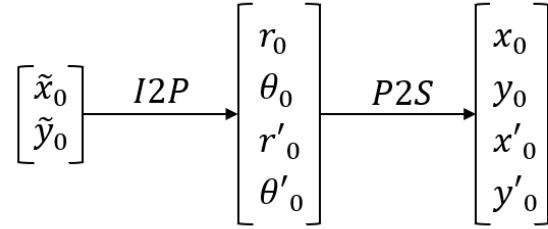


Figure 5.7: Coordinates transformation.

I2P is the function that maps each grid point position from the inertial frame to polar one. Furthermore, it computes the other two components of the state vector assuming an eccentricity of the initial osculating orbit e and initial true anomaly f_0 [19].

$$I2P(\tilde{x}_0, \tilde{y}_0) = \begin{cases} r_0 = \sqrt{\tilde{x}_0^2 + \tilde{y}_0^2} \\ \theta_0 = \arctan\left(\frac{\tilde{y}_0}{\tilde{x}_0}\right) \\ r'_0 = -\frac{r_0 e_p \sin(f_0)}{1 + e_p \cos(f_0)} \\ \theta'_0 = \sqrt{\frac{\mu(1+e)}{r_0^3(1+e_p \cos(f_0))}} - 1 \end{cases} \quad (5.11)$$

P2S is the function that converts each grid point from polar coordinates in Cartesian ones for the synodic frame.

$$P2S(r_0, \theta_0, r'_0, \theta'_0) = \begin{cases} x_0 = 1 + \mu + r_0 \cos(\theta_0) \\ y_0 = r_0 \sin(\theta_0) \\ x'_0 = r'_0 \cos(\theta_0) - r\theta'_0 \sin(\theta_0) \\ y'_0 = r'_0 \sin(\theta_0) + r\theta'_0 \cos(\theta_0) \end{cases} \quad (5.12)$$

Each IC is then integrated in a given anomalies interval with a 7th/8th order Runge-Kutta scheme [39]. The integration tolerance is set to 10^{-9} . Selected parameters for the computation of the initial states and Sun–Mars physical parameters are reported in Tab. 5.2.

Table 5.2: Parameters for the computation of the initial states and physical parameters.

Grid parameter	Value	Unit	Description
U	$[-6 \cdot 10^{-4}, 6 \cdot 10^{-4}] \times$ $[-6 \cdot 10^{-4}, 6 \cdot 10^{-4}]$	$[-]$	Computational domain boundaries $[x_{left}, x_{right}] \times [y_{down}, y_{up}]$
N	$25 \cdot 10^4$	$[-]$	Number of grid points
Initial condition	Value	Unit	Description
e	0.9	$[-]$	Eccentricity of osculating orbit
f_0	0	[rad]	Initial true anomaly
Physical parameter	Value	Unit	Description
μ	$3.2262008 \cdot 10^{-7}$	$[-]$	Mass parameter [19]
a_p	1.523688	[AU]	Sun–Mars semi-major axis [19]
e_p	0.093418	$[-]$	Sun–Mars eccentricity [19]
R_{eq}	3397	[km]	Mars mean equatorial radius [19]
R_s	$170 \cdot R_{eq}$	[km]	Mars SOI radius [24]

Initial states are propagated in the $[f_0, f_f]$ interval. LD scalar values are computed exploiting the state vector augmentation procedure described in Section 4.5. At the same time the classification algorithm categorize each IC into the subset $\mathcal{W}(f_f)$, $\mathcal{X}(f_f)$, or $\mathcal{K}(f_f)$. Separatrices are extracted from the contour plot of the descriptor field with the edge detection algorithm. Patterns are then overlapped to the computational grid classification, in which each subset is marked with a different colour. This allows to perform a visual check of the matching between WSBs and separatrices extracted from LD fields.

6 | Results

Results of the methodology described in the previous chapter are presented. Computational domain classifications and LD fields are visualized for the chosen phase space region around Mars. Different edge extraction methods are compared. Finally, the extracted separatrices are validated by overlapping them to different classification sets and verifying the correspondence with WSBs.

6.1. Classification sets

Each grid point inside the computational domain is classified into a specific subset (\mathcal{X} , \mathcal{K} or \mathcal{W}) depending on the nature of its trajectory and according to the integration interval. The initial true anomaly is kept fixed ($f_0 = 0$) and each IC is propagated up to f_f . Therefore, subsets are highly dependent on the final true anomaly and it assumes an important role in the classification step. Fig. 6.1 displays a visual representation of the classification for the whole computational grid for different values of f_f . Positive values of final anomaly indicate that the computational grid is propagated in forward time. An $f_f < 0$ reveals trajectories behaviour when ICs are integrated backward. The three complementary subsets $\mathcal{X}(f_f)$, $\mathcal{K}(f_f)$ and $\mathcal{W}(f_f)$ are marked with a different colour. Fig. 6.2 shows two different capture sets $\mathcal{C}(-\pi/2, 3\pi/2)$ and $\mathcal{C}(-\pi, 3\pi)$. Each IC belonging to the capture sets generates a ballistic capture orbit.

Weakly stable sets $\mathcal{W}(f_f)$ resemble stable sets \mathcal{W}_n presented in Fig. 5.2 and computed with the methodology described in [19]. However, keep note that the two stable sets definitions are considerably different. Stable sets in [19] are computed counting the number of revolutions around Mars in the synodic frame. A stable set \mathcal{W}_n contains ICs that perform n complete revolutions around the target while maintaining a negative Kepler energy at each revolution. Differently, the classification algorithm implemented in this research analyzes particle dynamics at fixed f_f and does not take into account stability number n . Besides that, a similarity between the two stable set definitions can be noticed for some values of f_f .

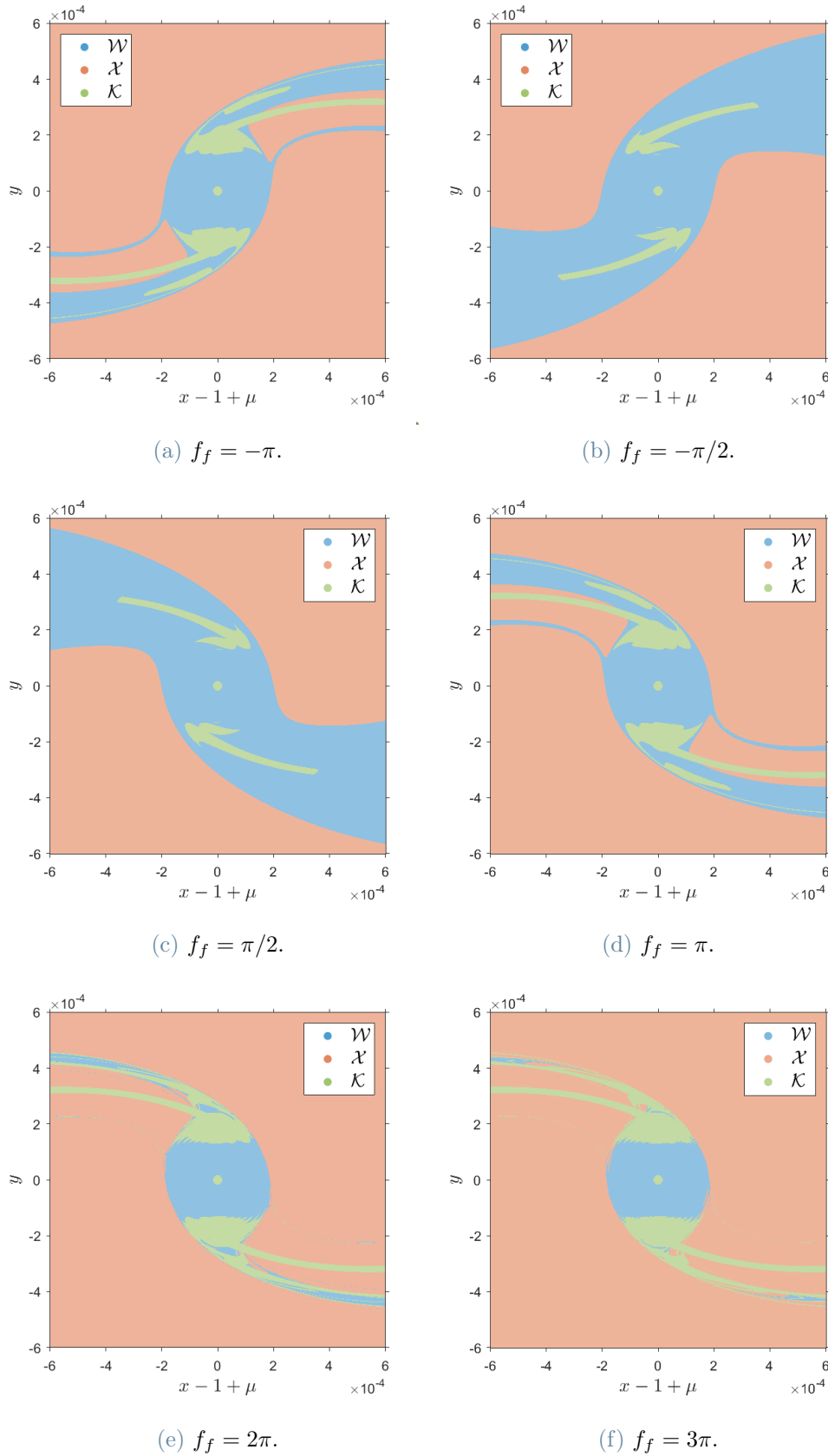


Figure 6.1: Computational grid classification for different values of f_f .

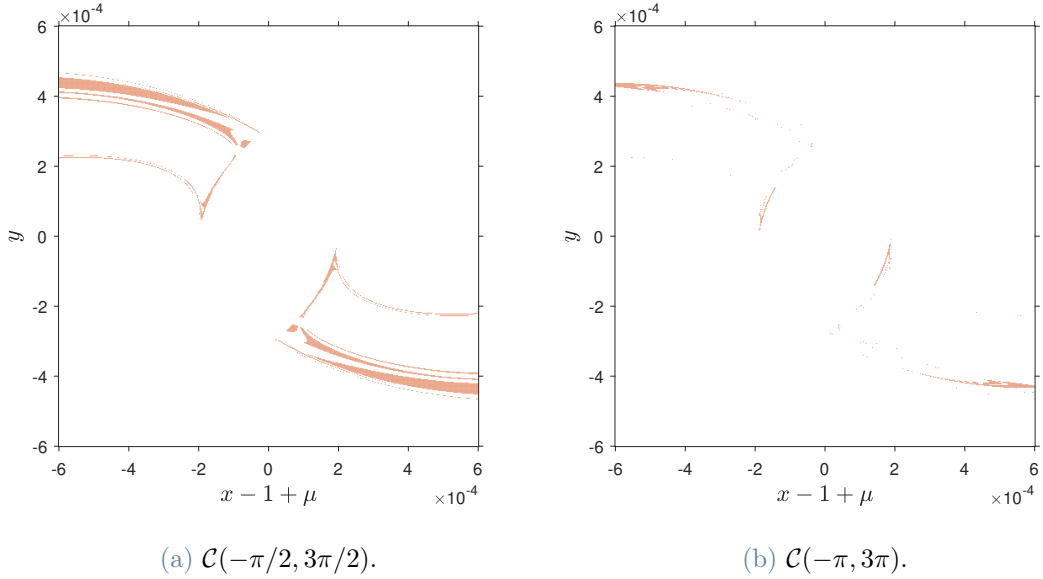


Figure 6.2: Two capture sets.

6.2. Lagrangian descriptor fields

Descriptor fields are computed according to the methodology described in Section 5.2. Contour plots of the five implemented descriptors (see Tab. 5.1) are presented in Fig. 6.3. The comparison between the different LDs is done for the same integration interval. All the descriptors reveal similar singular structures in the phase space, with the exception of M_5 , in which separation between regions is not so clear. Although not very visible in M_2 and M_4 fields, the structures are present and can be highlighted by scaling the fields with deamplification coefficients. Specifically, for M_2 , a scaling of $(M_2)^{0.1}$ is adopted (see Fig. 6.4a). Similarly, for M_4 , a $(M_4)^{0.3}$ deamplification is chosen. The scalar field is shown in Fig. 6.4b.

The M_3 descriptor underlines phase space regions separation in a clearer way if compared with the other indicators and is taken as reference in the separatrices extraction step. Fig. 6.5 displays M_3 fields for different integration intervals both in forward and backward time. As expected, the higher the value of f_F , the more structures are revealed. An high value of f_F gives to trajectories enough time to manifest their qualitative behaviour.

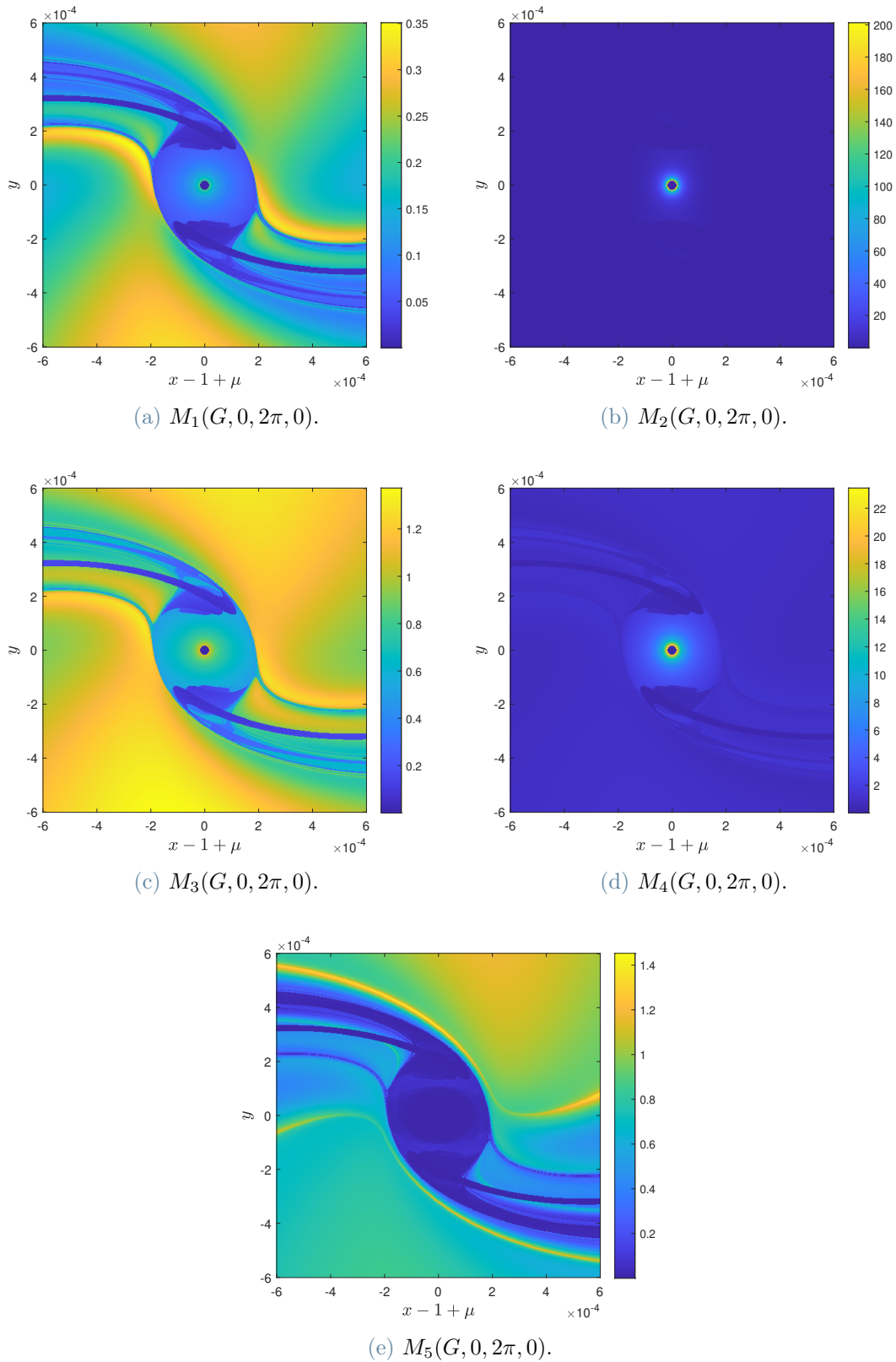
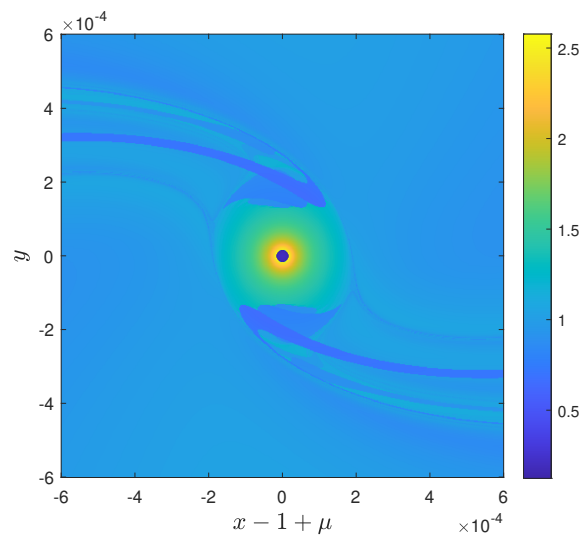
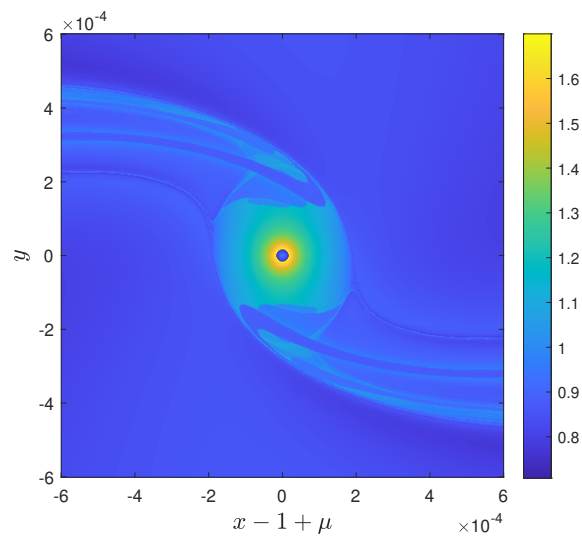
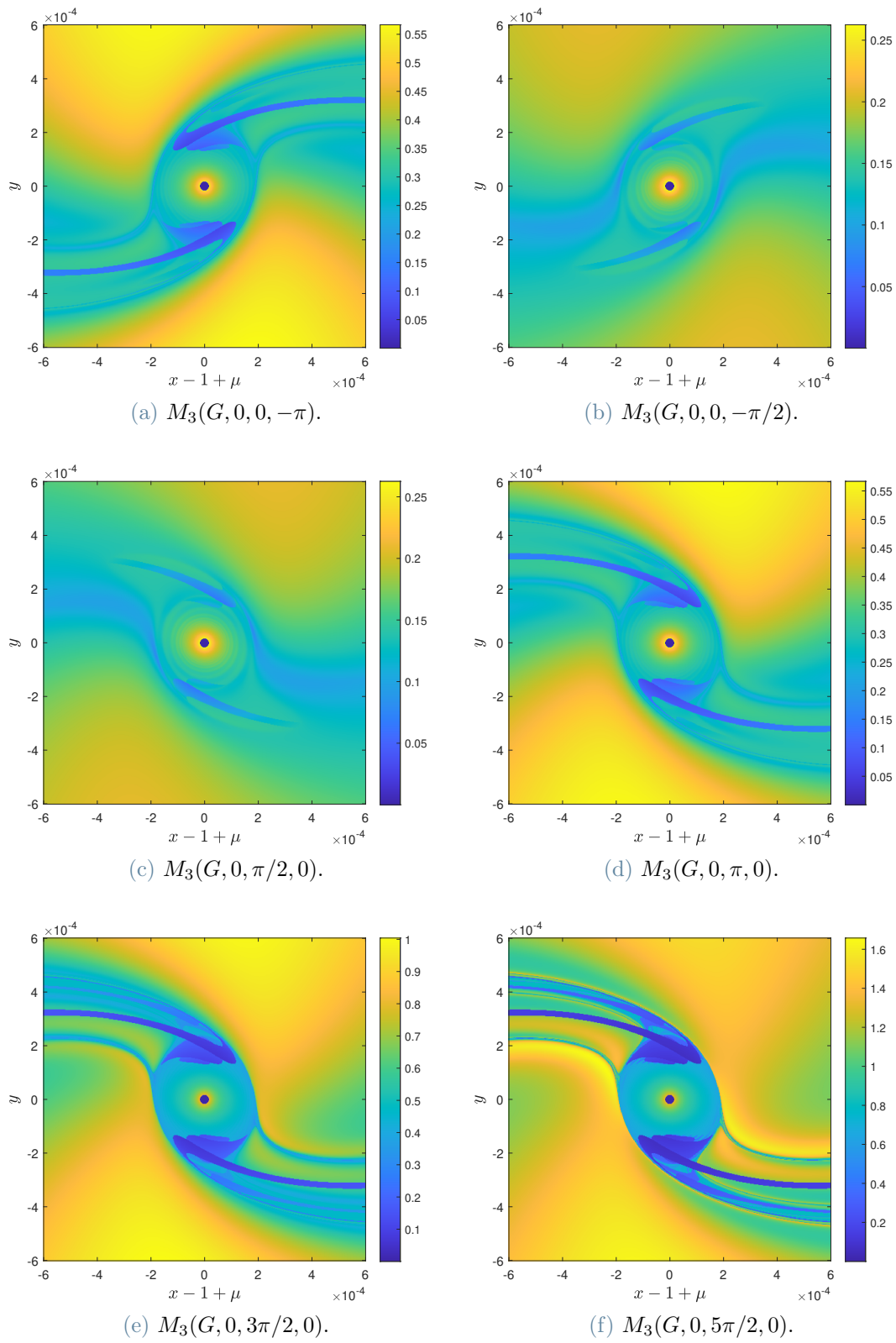


Figure 6.3: Comparison between LD fields computed for the same integration interval.

Figure 6.4: Scaled M_2 and M_4 fields.

Figure 6.5: $M_3(G, f_0, f_F, f_B)$ fields.

Notice that $M_3(G, 0, 0, f_B)$ and $M_3(G, 0, f_F, 0)$ are symmetric with respect to the x -axis if $|f_F| = |f_B|$. The explanation is implicit in the symmetry of ER3BP equations of motion. It is possible to check that the mapping $(x, y, x', y', f) \mapsto (x, -y, -x', y', -f)$ is a symmetry of Eq. (2.9) [11]. Two ICs symmetric with respect the x -axis satisfy the mapping if one condition is integrated forward ($f > 0$) and the other one backward ($f < 0$). It follows that the LD value associated to both conditions will be the same. The reasoning is valid only if $f_0 = k\pi$, with k any integer number. This also ensures the symmetry of the primaries. A more detailed explanation is reported in appendix A.

6.3. Extracted separatrices

As already introduced in Section 5.3, singular structures of LD contour plots are extracted with an edge detection algorithm. Sobel, Roberts, Canny and zero-cross methods are tested on the same descriptor field as shown in Fig. 6.6. Threshold value σ has not been specified for this comparison, letting the algorithms to choose σ autonomously. Note that in Fig. 6.6d two threshold values are specified. This is because the Canny method uses two thresholds to detect strong and weak edges. Specifically, the method starts with the higher threshold and then decreases it to include also the lower threshold result. This helps to fill in the gaps in the edges detected by the higher threshold [1]. As anticipated, Roberts method outputs the separatrices in a clearer way compared with the other methods, limiting the presence of false positives in the binary image. Once the method has been selected, threshold is then tuned as described in Section 5.3. Tab. 6.1 reports chosen thresholds associated to computed LD fields. Extracted dynamics separatrices obtained with the tuned thresholds for some LD fields are shown in Fig. 6.7

Table 6.1: Computed descriptor fields and associated thresholds.

LD field	σ
$M_3(G, 0, \pi/2, 0)$	$4 \cdot 10^{-3}$
$M_3(G, 0, \pi, 0)$	$6 \cdot 10^{-3}$
$M_3(G, 0, 3\pi/2, 0)$	$9 \cdot 10^{-3}$
$M_3(G, 0, 2\pi, 0)$	$20 \cdot 10^{-3}$
$M_3(G, 0, 5\pi/2, 0)$	$25 \cdot 10^{-3}$
$M_3(G, 0, 3\pi, 0)$	$30 \cdot 10^{-3}$
$M_3(G, 0, 0, -\pi/2)$	$4 \cdot 10^{-3}$
$M_3(G, 0, 0, -\pi)$	$6 \cdot 10^{-3}$

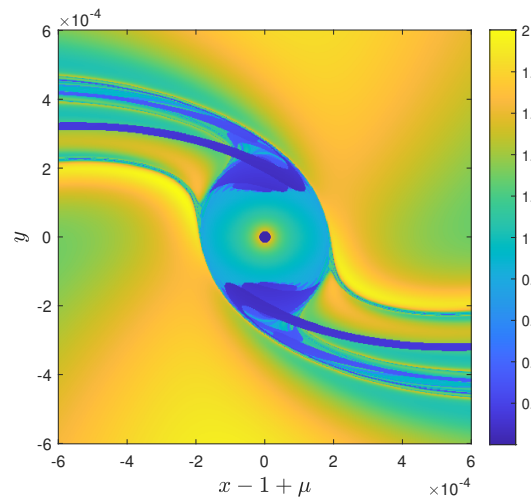
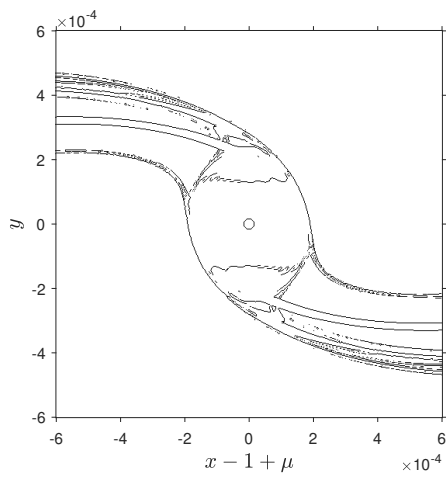
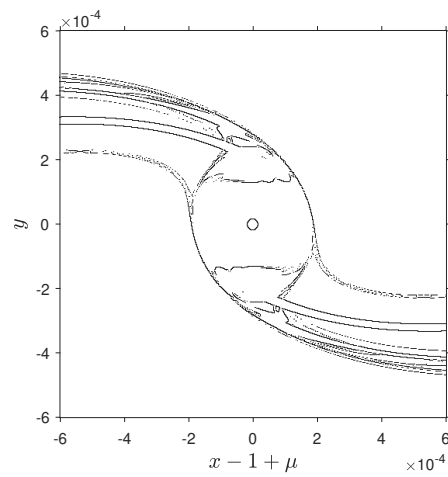
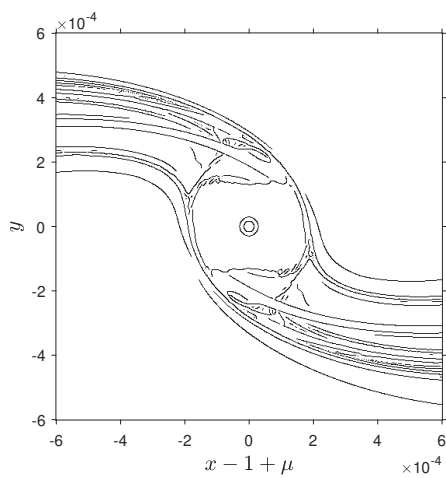
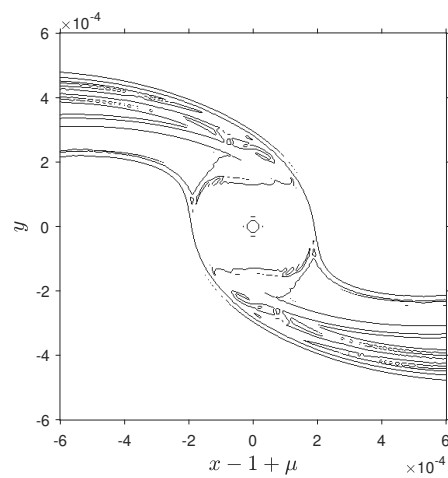
(a) $M_3(G, 0, 3\pi, 0)$.(b) Sobel ($\sigma = 0.1599$).(c) Roberts ($\sigma = 0.1599$).(d) Canny ($\sigma = 0.0125, 0.0312$).(e) Zero-cross ($\sigma = 0.0041$).

Figure 6.6: Edge detection methods comparison.

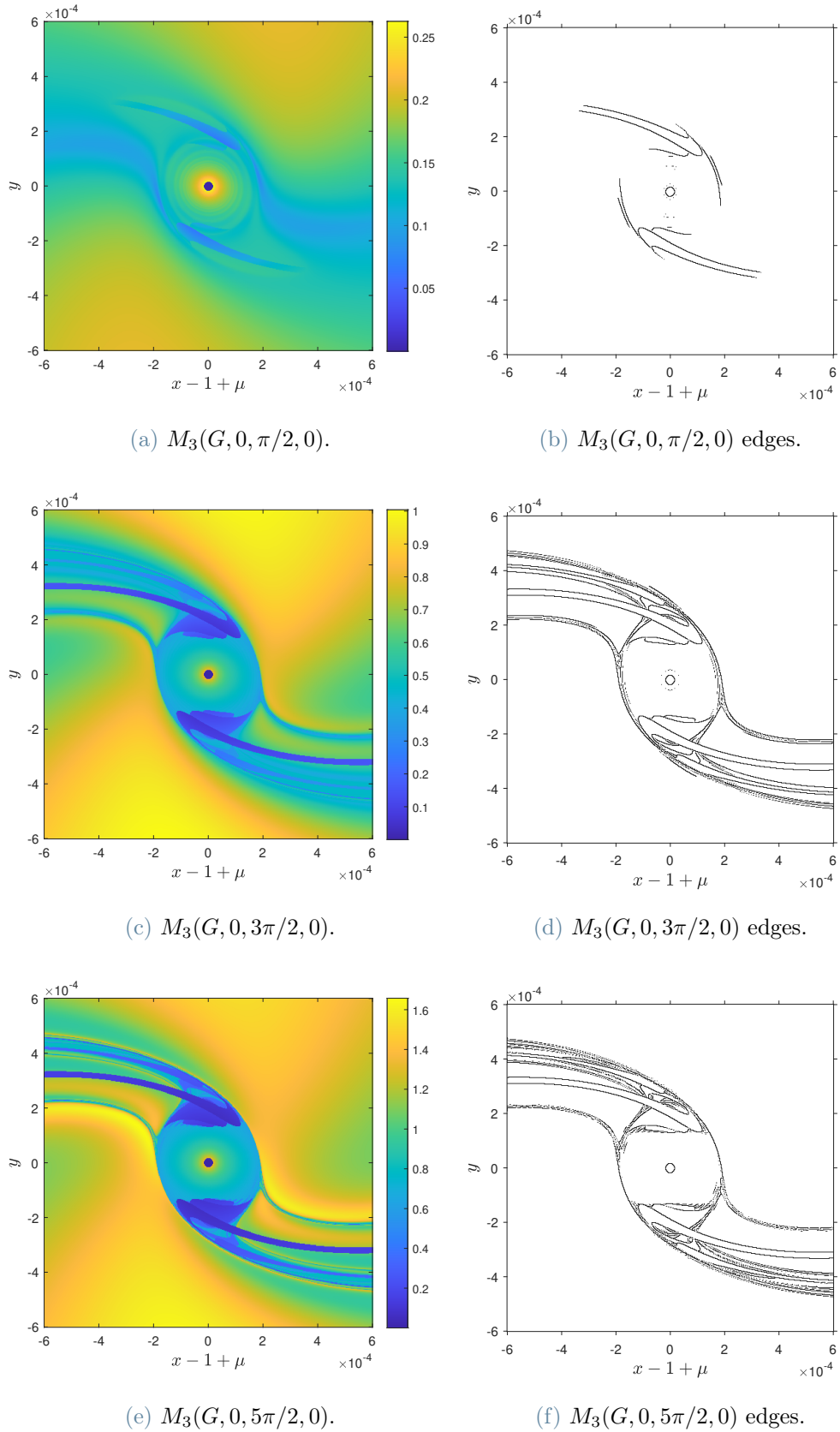


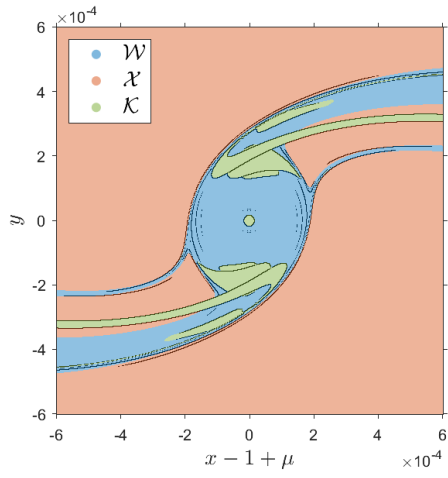
Figure 6.7: $M_3(G, f_0, f_F, f_B)$ fields with extracted separatrices.

6.4. Validation

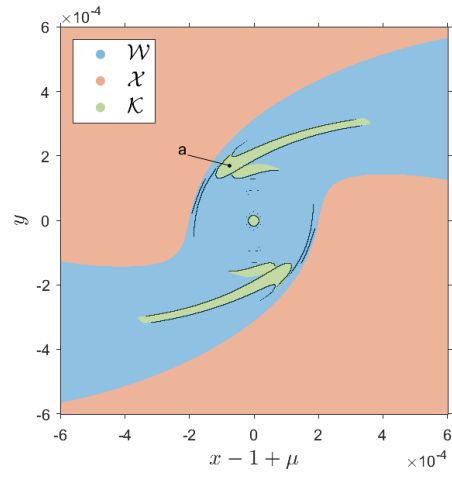
Correspondence between extracted patterns and WSB is tested for different integration intervals. Fig. 6.8 shows the extracted patterns from edge algorithm overlapped to \mathcal{X} , \mathcal{K} , and \mathcal{W} subsets. A good match of separatrices with boundaries of classified regions can be noticed. Two key points deserve mention. First of all, the correspondence is not always perfect, especially for small values of f_f . The cause is implied in the descriptor definition. LD reveals patterns if ICs are integrated long enough for dynamic divergences between the orbits to be appreciated. It may happen that the classification algorithm divides a particular region of the phase space into two different subsets, but the orbits are not so divergent to generate singular structures in the LD field. In this case we expect an high gradient in the field in correspondence of the WSB, but not sufficiently high to be detected by the edge detection algorithm. Secondly, the LD may detect divergence in dynamic behaviour even in areas that are classified in the same way. For instance, two grid points can both generate escape orbits, but trajectories could be very different from each other. This usually happens at higher values of f_f .

Combining LD structures obtained propagating dynamics forwards with the ones obtained propagating backwards, it is possible to reveal patterns that rule particles transport in both time directions. The correlation of two different capture sets $\mathcal{C}(f_B, f_F)$ with extracted patterns from $M_3(G, 0, f_F, f_B)$ can be recognized in Fig. 6.9. Some regions in the phase space which are enclosed by LD separatrices correspond to the capture set. The presented methodology shows the ability of LDs in underlining phase space regions associated to a set $\mathcal{C}(f_B, f_F)$. ICs belonging to this set generate orbits that approach Mars and remain temporary captured at least for f_F . For instance, if $f_F = 3\pi$, particle will remain bounded into Mars influence at least for three semi-revolutions of the planet around the Sun. However, the identification of ballistic capture regions is not trivial. For a practical use of the LD methodology in the design of ballistic capture orbits, it is necessary to have a tool for classifying the trajectories generated from a region enclosed by dynamics separatrices.

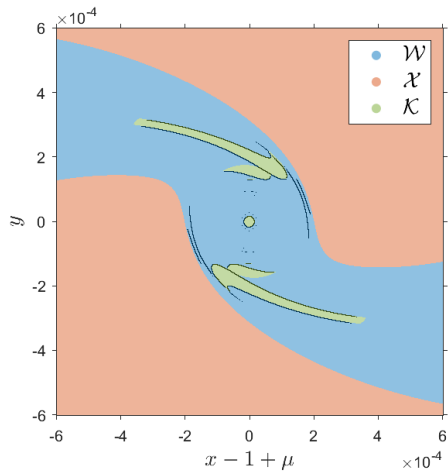
Some ICs are sampled from Figs. 6.8 and 6.9 and collected in Tab. 6.2. Orbits generated from these samples are shown in Figs. 6.10 and 6.11 in the Mars-centered inertial frame. It is clear how the behaviour of each orbit corresponds to the set the IC belongs to. Moreover, the importance of f_f in the classification procedure is highlighted. Samples "c" and "d" (see Fig. 6.8d) are classified into two different sets, but their dynamics is similar, as seen from generated orbits. For a slightly larger f_f , both orbits escape from Mars.



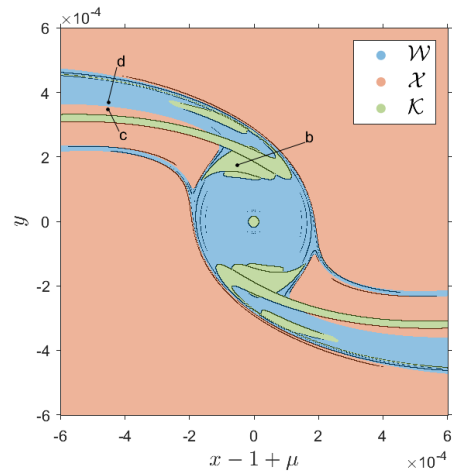
(a) $M_3(G, 0, 0, -\pi)$.



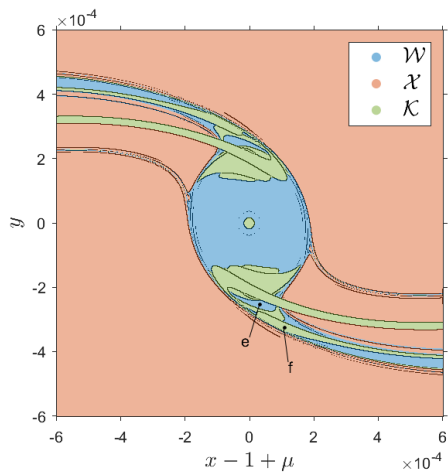
(b) $M_3(G, 0, 0, -\pi/2)$.



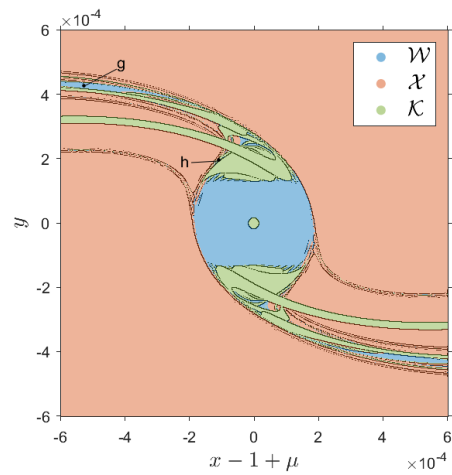
(c) $M_3(G, 0, \pi/2, 0)$.



(d) $M_3(G, 0, \pi, 0)$.

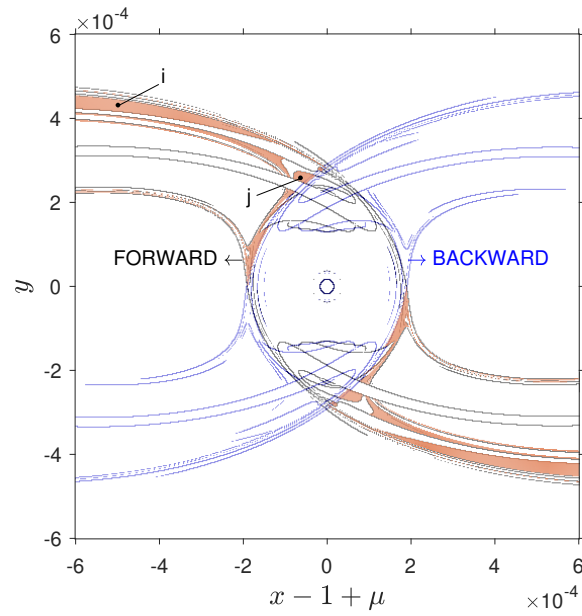


(e) $M_3(G, 0, 3\pi/2, 0)$.

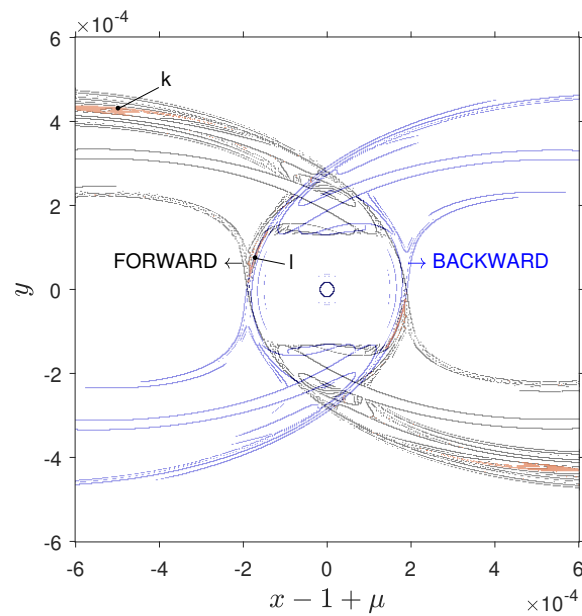


(f) $M_3(G, 0, 5\pi/2, 0)$.

Figure 6.8: Extracted separatrices overlapped to subsets for different final anomalies.



(a) $M_3(G, 0, 3\pi/2, -\pi)$ separatrices and $\mathcal{C}(-\pi, 3\pi/2)$.



(b) $M_3(G, 0, 3\pi, -\pi)$ separatrices and $\mathcal{C}(-\pi, 3\pi)$.

Figure 6.9: Extracted separatrices overlapped to capture sets. Gray lines are associated with the forward branch of the integral and blue lines with the backward one.

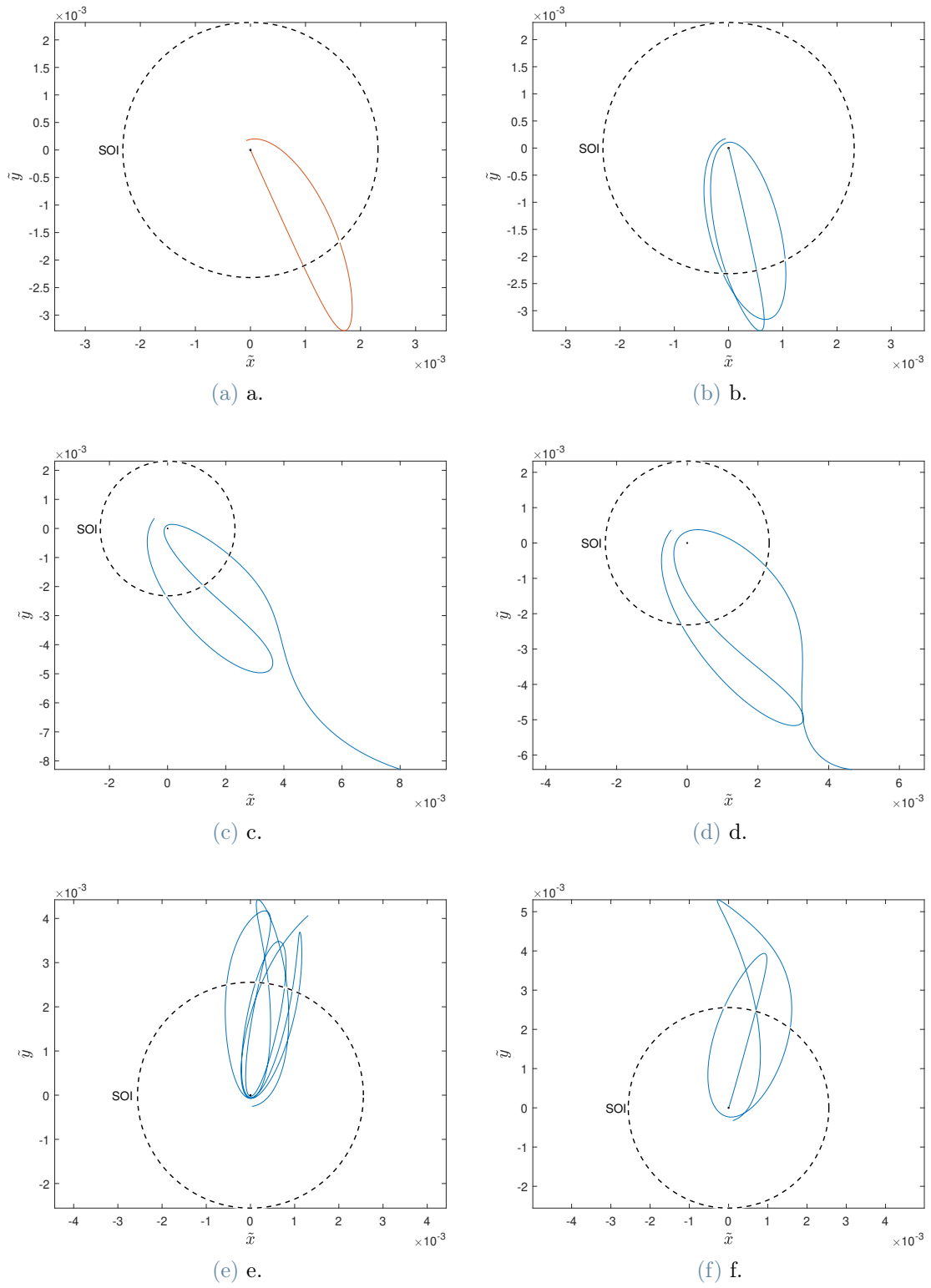


Figure 6.10: Orbits generated from samples "a" to "f" in Tab. 6.2 (red path: backwards propagation; blue path: forwards propagation).

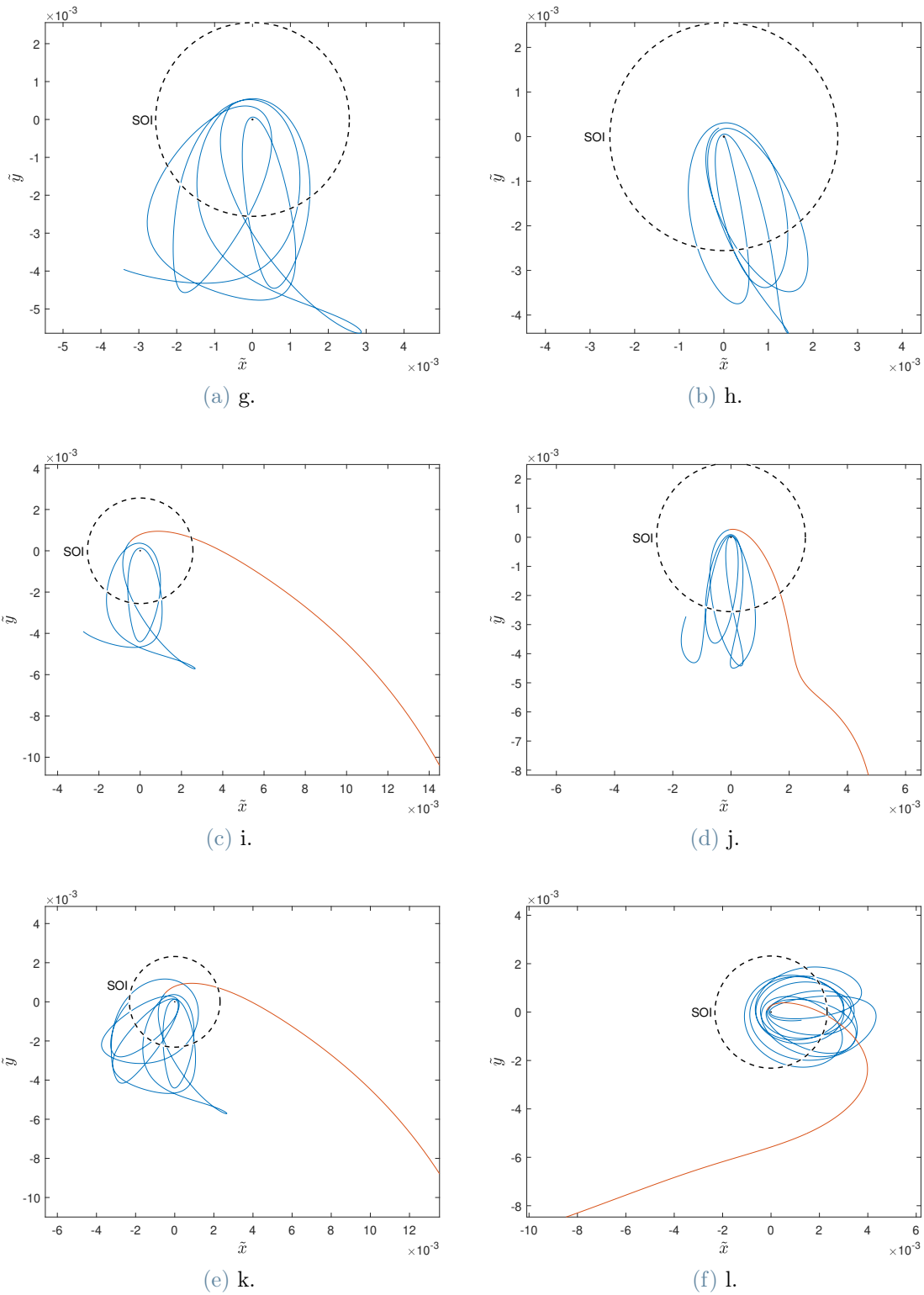


Figure 6.11: Orbits generated from samples "g" to "l" in Tab. 6.2 (red path: backwards propagation; blue path: forwards propagation).

Table 6.2: Initial conditions sampled from Figs. 6.8 and 6.9.

Label	\tilde{x}_0	\tilde{y}_0	Set
a	$-7.575 \cdot 10^{-5}$	$1.695 \cdot 10^{-4}$	$\mathcal{K}(-\pi/2)$
b	$-5.170 \cdot 10^{-5}$	$1.743 \cdot 10^{-4}$	$\mathcal{K}(\pi)$
c	$-4.533 \cdot 10^{-4}$	$3.475 \cdot 10^{-4}$	$\mathcal{X}(\pi)$
d	$-4.509 \cdot 10^{-4}$	$3.691 \cdot 10^{-4}$	$\mathcal{W}(\pi)$
e	$3.246 \cdot 10^{-5}$	$-2.537 \cdot 10^{-4}$	$\mathcal{W}(3\pi/2)$
f	$1.094 \cdot 10^{-4}$	$-3.258 \cdot 10^{-4}$	$\mathcal{K}(3\pi/2)$
g	$-5.278 \cdot 10^{-4}$	$4.268 \cdot 10^{-4}$	$\mathcal{W}(5\pi/2)$
h	$-1.094 \cdot 10^{-4}$	$1.960 \cdot 10^{-4}$	$\mathcal{K}(5\pi/2)$
i	$-4.990 \cdot 10^{-4}$	$4.317 \cdot 10^{-4}$	$\mathcal{C}(-\pi, 3\pi/2)$
j	$-6.373 \cdot 10^{-5}$	$2.585 \cdot 10^{-4}$	$\mathcal{C}(-\pi, 3\pi/2)$
k	$-4.990 \cdot 10^{-4}$	$4.317 \cdot 10^{-4}$	$\mathcal{C}(-\pi, 3\pi)$
l	$-1.719 \cdot 10^{-4}$	$7.575 \cdot 10^{-5}$	$\mathcal{C}(-\pi, 3\pi)$

7 | Conclusions

This study work wants to answer the following research question:

To what extent Lagrangian descriptors provide a characterization of the dynamics in Mars proximity with regard to ballistic capture?

As shown in the results, structures in the phase space detected by LDs are able to distinguish regions characterized by different dynamical behaviour. In particular, at different integration intervals, the patterns extracted with the edge detection algorithm delimit with good approximation the ICs that generate differently classified orbits. Extracted dynamics separatrices adequately match with the WSBs. Similarly, the LD approach detects areas corresponding to capture regions with reasonable approximation. The explanation of this correspondence is intuitive. The descriptor value associated with an IC identifies a characteristic property of the generated orbit, such as the trajectory length [26]. Orbits with qualitatively different behaviour are then associated to a different value of the descriptor. As result, the WSB of a classification set is linked with an abrupt change in the scalar value of the field.

LD capability in the detection of the WSB has proved better than other LCS-based approaches applied to ballistic capture [31, 33]. Approaches to extract dynamics separatrices like FTLE and variational theory require the integration of the variational equations associated to the dynamic model. In general, this is computationally more intensive than propagating the augmented dynamics to compute the descriptor. Moreover, as shown in Section 4.7, the identification WSB with FTLE or the variational theory is tougher. Differently, the WSB appears well resolved when exploiting LDs-based techniques.

The main drawback of the LD approach is that it does not give information about which, among the different regions bounded by the separatrices, are actually capture or stable sets. This is a limitation in the application of the presented LD methodology to the design of ballistic capture orbits. The procedure of computing the LD fields, together with extraction and validation of the dynamics separatrices have had a positive response. Thus, based on the obtained results, a viable strategy to design ballistic capture orbits is proposed. A possible solution could be to categorize the various regions delimited by

the extracted separatrices by sampling a few ICs and classifying their orbits. In this way, each region in the phase space can be classified on the basis of its qualitative behaviour (weakly stable, escape, capture, or impact). The assumption under this procedure is that each IC of a phase space region bounded by separatrices belongs to the same classification set.

In conclusion, LD proved to be an intuitive, easy to implement and computationally efficient visual tool. Without any a priori knowledge, LD patterns yield a strong match with the WSB of classification sets. The LD approach supports the design of ballistic capture trajectories, enriching the dynamics knowledge in proximity of the target planet.

Recommendations for future work

In this work different LDs have been implemented and tested in the context of Sun–Mars planar ER3BP. However, further studies may be done on other integrands in the descriptor definition. The goal may be to find a LD that separates regions in the phase space more clearly than the proposed descriptors.

As discussed, the final true anomaly f_f set as integration limit for each IC has an important role. The proposed methodology is based on the utilization of a constant f_f within the domain of the initial states. The thesis shows also that a variable f_f inside the domain could lead to better results in the extraction of the WSB of some stable sets (see Section 5.2.1). This aspect deserves to be analyzed more in details.

In this research, the initial true anomaly f_0 and eccentricity e of initial osculating orbits about Mars are kept fixed. It would be interesting to study how the LD fields vary with these parameters. Moreover, an additional research on edge detection methods and sensitivity thresholds selection would improve the proposed methodology.

Finally, the presented research work could be used as basis for further applications of the method in more complex astrodynamical models. An important advantage is that the LD method can be applied to arbitrary complex dynamical systems without restrictions. Thus, the presented approach could be generalized for the application in real solar systems models such as the n -body problem including different orbital perturbations.

A | LD fields symmetry

This appendix gives a mathematical proof of the fact that $M(G, f_0, 0, f_B)$ and $M(G, f_0, f_F, 0)$ are symmetric with respect to the x -axis if $|f_F| = |f_B|$ and $f_0 = k\pi$, with k any integer number.

ER3BP equations of motion can be manipulated as follows

$$\begin{cases} x'' - 2y' = \omega_x, \\ y'' + 2x' = \omega_y, \end{cases} \quad (\text{A.1})$$

$$\begin{cases} x'' - 2y' = \left(x - \frac{(1-\mu)(x+\mu)}{r_1^3} - \frac{\mu(x-1+\mu)}{r_2^3} \right) \frac{1}{1+e_p \cos(f)}, \\ y'' + 2x' = \left(y - \frac{(1-\mu)y}{r_1^3} - \frac{\mu y}{r_2^3} \right) \frac{1}{1+e_p \cos(f)}. \end{cases} \quad (\text{A.2})$$

By substituting the variables $(x, -y, -x', y', -f)$ in the system, the same equations are retrieved. In other words, the dynamics is not changed. Thus, the mapping $(x, y, x', y', f) \mapsto (x, -y, -x', y', -f)$ is a symmetry of the ER3BP.

Each particle in the computational domain is initially set at the periapsis of a Keplerian orbit around Mars with same eccentricity e . It follows that two conditions \mathbf{x}_1 and \mathbf{x}_2 initially placed symmetrically with respect to the x -axis have initial states of $\mathbf{x}_1 = [x_0, y_0, x'_0, y'_0]$ and $\mathbf{x}_2 = [x_0, -y_0, -x'_0, y'_0]$. Assume that \mathbf{x}_1 is integrated forward in $[0, \bar{f}]$ interval and \mathbf{x}_2 is propagated backward in $[0, -\bar{f}]$ interval. Recalling the mapping reported before, the two conditions will be subjected to the same dynamics and their trajectories will be symmetric about the x -axis.

Since LDs are based on the integration of the norm of a quantity related to the state, e.g. $[x', y']$, the descriptor value associated to both conditions will be the same. This is valid only if $f_0 = k\pi$, with k any integer number. This guarantees the symmetry of the primaries.

Bibliography

- [1] S. Ansari, S. Prabhu, N. Kini, G. Hegde, and Y. Haider. “A Survey on Conventional Edge Detection Techniques”. In: *International Journal of Scientific Research in Computer Science Applications and Management Studies* 3 (2014) (cit. on pp. 44, 55).
- [2] E. Belbruno, M. Gidea, and F. Topputo. “Weak Stability Boundary and Invariant Manifolds”. In: *SIAM J. Applied Dynamical Systems* 9 (2010), pp. 1061–1089. DOI: 10.1137/090780638 (cit. on pp. 6–8).
- [3] E. A. Belbruno and J. K. Miller. “Sun-perturbed Earth-to-moon transfers with ballistic capture”. In: *Journal of Guidance, Control, and Dynamics* 16.4 (1993), pp. 770–775. DOI: 10.2514/3.21079 (cit. on p. 2).
- [4] S. Campagnola, B. B. Buffington, and A. E. Petropoulos. “Jovian tour design for orbiter and lander missions to Europa”. In: *Acta Astronautica* 100 (2014), pp. 68–81. ISSN: 0094-5765. DOI: 10.1016/j.actaastro.2014.02.005 (cit. on p. 2).
- [5] M. Chupin, T. Haberkorn, and E. Trélat. “Transfer Between Invariant Manifolds: From Impulse Transfer to Low-Thrust Transfer”. In: *Journal of Guidance, Control, and Dynamics* 41.3 (2018), pp. 658–672. DOI: 10.2514/1.G002922 (cit. on p. 8).
- [6] J. Elliott and L. Alkalai. “Lunette: A network of lunar landers for in-situ geophysical science”. In: *Acta Astronautica* 68 (2011), pp. 1201–1207. DOI: 10.1016/j.actaastro.2010.10.024 (cit. on p. 2).
- [7] M. Farazmand and G. Haller. “Computing Lagrangian coherent structures from their variational theory”. In: *Chaos: An Interdisciplinary Journal of Nonlinear Science* 22.1 (2012), p. 013128. DOI: 10.1063/1.3690153 (cit. on pp. 25, 28, 35).
- [8] V. García Garrido. “A Tutorial on the Method of Lagrangian Descriptors”. 2019. DOI: 10.6084/m9.figshare.11340818.v2 (cit. on p. 29).
- [9] V. J. García-Garrido, J. Curbelo, C. R. Mechoso, A. M. Mancho, and S. Wiggins. “A simple kinematic model for the Lagrangian description of relevant nonlinear processes in the stratospheric polar vortex”. In: *Nonlinear Processes in Geophysics* 24.2 (2017), pp. 265–278. DOI: 10.5194/npg-24-265-2017 (cit. on p. 29).

- [10] V. J. García-Garrido, A. Ramos, A. M. Mancho, J. Coca, and S. Wiggins. “A dynamical systems perspective for a real-time response to a marine oil spill”. In: *Marine Pollution Bulletin* 112.1 (2016), pp. 201–210. ISSN: 0025-326X. DOI: 10.1016/j.marpolbul.2016.08.018 (cit. on p. 29).
- [11] E. Gawlik, J. Marsden, P. Du Toit, and S. Campagnola. “Lagrangian coherent structures in the planar elliptic restricted three-body problem”. In: *Celestial Mechanics and Dynamical Astronomy* 103 (2009), pp. 227–249. DOI: 10.1007/s10569-008-9180-3 (cit. on pp. 11, 33, 55).
- [12] F. Gonzalez Montoya and S. Wiggins. “Phase space structure and escape time dynamics in a Van der Waals model for exothermic reactions”. In: *Physical Review E* 102.6 (2020). ISSN: 2470-0053. DOI: 10.1103/physreve.102.062203 (cit. on p. 29).
- [13] G. Haller and G. Yuan. “Lagrangian coherent structures and mixing in two-dimensional turbulence”. In: *Physica D: Nonlinear Phenomena* 147.3 (2000), pp. 352–370. ISSN: 0167-2789. DOI: 10.1016/S0167-2789(00)00142-1 (cit. on pp. 19, 27).
- [14] G. Haller. “Lagrangian Coherent Structures”. In: *Annual Review of Fluid Mechanics* 47.1 (2015), pp. 137–162. DOI: 10.1146/annurev-fluid-010313-141322 (cit. on pp. 3, 19, 20, 23, 27).
- [15] G. Haller. “Lagrangian coherent structures from approximate velocity data”. In: *Physics of Fluids* 14 (2002), pp. 1851–1861. DOI: 10.1063/1.1477449 (cit. on pp. 20, 22).
- [16] G. Haller. “Variational Theory of Hyperbolic Lagrangian Coherent Structures”. In: *Physica D-nonlinear Phenomena* 240 (2011). DOI: 10.1016/j.physd.2010.11.010 (cit. on pp. 19, 20, 23, 25–27).
- [17] G. Haller and T. Sapsis. “Lagrangian coherent structures and the smallest finite-time Lyapunov exponent”. In: *Chaos (Woodbury, N.Y.)* 21 (2011), p. 023115. DOI: 10.1063/1.3579597 (cit. on pp. 22, 25).
- [18] S. Hatch, M.-k. Chung, J. Kangas, S. Long, R. Roncoli, and T. Sweetser. “Trans-Lunar Cruise Trajectory Design of GRAIL (Gravity Recovery and Interior Laboratory) Mission”. In: *AIAA/AAS Astrodynamics Specialist Conference*. 2010. ISBN: 978-1-62410-150-2. DOI: 10.2514/6.2010-8384 (cit. on p. 2).
- [19] N. Hyeraci and F. Topputo. “Method to Design Ballistic Capture in the Elliptic Restricted Three-Body Problem”. In: *Journal of Guidance, Control, and Dynamics* 33 (2010), pp. 1814–1823. DOI: 10.2514/1.49263 (cit. on pp. 1, 2, 11–14, 17, 34, 35, 38–41, 45–47, 49).
- [20] R. Jehn, S. Campagnola, D. García Yáñez, and S. Kemble. “Low-thrust approach and gravitational capture at Mercury”. In: *18th International Symposium on Space Flight Dynamics*. 2004, pp. 487–492 (cit. on p. 2).

- [21] W. S. Koon, M. W. Lo, J. E. Marsden, and S. D. Ross. “Dynamical Systems, the Three-Body Problem and Space Mission Design”. In: *Equadiff 99*. World Scientific Publishing Company, 2011, pp. 1167–1181. DOI: 10.1142/9789812792617_0222 (cit. on pp. 1, 2, 5–10, 13).
- [22] C. Lopesino, F. Balibrea-Iniesta, V. J. García-Garrido, S. Wiggins, and A. M. Mancho. “A Theoretical Framework for Lagrangian Descriptors”. In: *International Journal of Bifurcation and Chaos* 27.01 (2017), p. 1730001. ISSN: 1793-6551. DOI: 10.1142/s0218127417300014 (cit. on pp. 30, 35).
- [23] Z.-F. Luo and F. Topputo. “Analysis of Ballistic Capture in Sun–Planet Models”. In: *Advances in Space Research* 56 (2015). DOI: 10.1016/j.asr.2015.05.042 (cit. on pp. 1, 15–17).
- [24] Z.-F. Luo, F. Topputo, F. Bernelli-Zazzera, and G.-J. Tang. “Constructing ballistic capture orbits in the real Solar System model”. In: *Celestial Mechanics and Dynamical Astronomy* 120 (2014), pp. 433–450. DOI: 10.1007/s10569-014-9580-5 (cit. on pp. 1, 13–16, 37, 47).
- [25] Z.-F. Luo and F. Topputo. “Mars orbit insertion via ballistic capture and aerobraking”. In: *ASTRODYNAMICS* 5 (2021), pp. 167–181. DOI: 10.1007/s42064-020-0095-4 (cit. on p. 1).
- [26] J. A. J. Madrid and A. M. Mancho. “Distinguished trajectories in time dependent vector fields.” In: *Chaos* 19 1 (2009). DOI: 10.1063/1.3056050 (cit. on pp. 29, 31, 65).
- [27] A. M. Mancho, S. Wiggins, J. Curbelo, and C. Mendoza. “Lagrangian descriptors: A method for revealing phase space structures of general time dependent dynamical systems”. In: *Communications in Nonlinear Science and Numerical Simulation* 18.12 (2013), pp. 3530–3557. ISSN: 1007-5704. DOI: 10.1016/j.cnsns.2013.05.002 (cit. on pp. 3, 20, 28–32, 35, 40).
- [28] M. Manzi. “A flow-informed strategy for ballistic capture trajectory design”. MSc thesis. Delft University of Technology, 2019 (cit. on pp. 3, 34).
- [29] C. Mendoza, A. Mancho, and S. Wiggins. “Lagrangian descriptors and the assessment of the predictive capacity of oceanic data sets”. In: *Nonlinear Processes in Geophysics* 21 (2014), pp. 677–689. DOI: 10.5194/npg-21-677-2014 (cit. on p. 29).
- [30] K. Padberg-Gehle, T. Hauff, F. Jenko, and O. Junge. “Lagrangian structures and transport in turbulent magnetized plasmas”. In: *New Journal of Physics* 9 (2007), p. 400. DOI: 10.1088/1367-2630/9/11/400 (cit. on p. 31).

- [31] A. S. Parkash. “Application of Lagrangian Coherent Structures to the computation and understanding of ballistic capture trajectories”. MSc thesis. Delft University of Technology, 2019 (cit. on pp. 3, 33, 34, 45, 65).
- [32] L. Roberts. *Machine Perception of Three-Dimensional Solids*. 1963. ISBN: 0-8240-4427-4 (cit. on p. 44).
- [33] X. R. Roca. “Computation of Lagrangian Coherent Structures with Application to Weak Stability Boundaries”. Bachelor thesis. Universitat Politècnica de Catalunya, 2015 (cit. on pp. 3, 21, 25, 34, 45, 65).
- [34] J. Schoenmaekers. “Post-launch Optimisation of the SMART-1 Low-thrust Trajectory to the Moon”. In: *18th International Symposium on Space Flight Dynamics*. Vol. 548. 2004, p. 505 (cit. on p. 2).
- [35] S. C. Shadden, F. Lekien, and J. E. Marsden. “Definition and properties of Lagrangian coherent structures from finite-time Lyapunov exponents in two-dimensional aperiodic flows”. In: *Physica D: Nonlinear Phenomena* 212.3 (2005), pp. 271–304. ISSN: 0167-2789. DOI: 10.1016/j.physd.2005.10.007 (cit. on pp. 22, 23).
- [36] F. Topputo and E. Belbruno. “Earth–Mars transfers with ballistic capture”. In: *Celestial Mechanics and Dynamical Astronomy* 121.4 (2015), pp. 329–346. ISSN: 1572-9478. DOI: 10.1007/s10569-015-9605-8 (cit. on pp. 11, 17, 18).
- [37] F. Topputo, M. Vasile, and F. Bernelli-Zazzera. “Low Energy Interplanetary Transfers Exploiting Invariant Manifolds of the Restricted Three-Body Problem”. In: *Journal of the Astronautical Sciences* 53.4 (2005), pp. 353–372. DOI: 10.1007/BF03546358 (cit. on pp. 9, 11).
- [38] H. Urrutxua, D. Scheeres, C. Bombardelli, J. L. Gonzalo, and J. Pelaez. “What does it take to capture an asteroid? A case study on capturing asteroid 2006 RH120”. In: *Advances in the Astronautical Sciences* 152 (2014), pp. 1117–1136 (cit. on p. 2).
- [39] J. Verner. “Numerically optimal Runge-Kutta pairs with interpolants”. In: *Numerical Algorithms* 53.2 (2010), pp. 383–396. DOI: 10.1007/s11075-009-9290-3 (cit. on p. 47).
- [40] M. Vetrivano, W. Van der Weg, and M. Vasile. “Navigating to the Moon Along Low-Energy Transfers”. In: *Celestial Mechanics and Dynamical Astronomy* 114 (2012). DOI: 10.1007/s10569-012-9436-9 (cit. on p. 2).
- [41] E. Zulli. “Understanding the 65803 Didymos dynamical environment applying Lagrangian coherent structures”. MSc thesis. Politecnico di Milano, 2021 (cit. on p. 3).